Real and complex valued geometrical optics inverse ray-tracing for inline field calculations

A. Colaitis, J. P Palastro, R. K Follett, I. V Igumenschev, V. Goncharov

Real and Complex valued Geometrical Optics Inverse Ray-Tracing for Inline Field Calculations

A. Colaïtis,[1,2] J. P. Palastro,[1] R. K. Follett,[1] I. Igumenschev,[1] and V. Goncharov[1]
[1)] *Laboratory for Laser Energetics, 250 East River Rd, Rochester, NY 14623-1212*
[2)] *now at Centre Lasers Intenses et Applications, UMR 5107, 351 Cours de la libération, 33400 Talence, France*

(Dated: 5 February 2019)

A 3-D ray based model for computing laser fields in dissipative and amplifying media is presented. The eikonal equation is solved using inverse ray-tracing on a dedicated nonstructured 3-D mesh. Inverse ray-tracing opens the possibility of using Complex Geometrical Optics (CGO), for which we propose a propagation formalism in a finite element mesh. Divergent fields at caustics are corrected using an etalon integral method for fold-type caustics. This method is successfully applied in dissipative media by modifying the ray-ordering and root selection rules, thereby allowing one to reconstruct the field in the entire caustic region. In addition, we demonstrate how caustics in the CGO framework can disappear entirely for sufficiently dissipative media, making the complex ray approach valid in the entire medium. CGO is shown to offer a more precise modeling of laser refraction and absorption in a dissipative medium when compared to Geometrical Optics (GO). In the framework of Inertial Confinement Fusion (ICF), this occurs mostly at intermediate temperatures or at high temperatures close to the critical density. Additionally, GO is invalid at low temperatures if an approximated expression of the permittivity is used. The inverse ray-tracing algorithm for GO and CGO is implemented in the *IFRIIT* code, in the framework of a dielectric permittivity described in 3-D using a piecewise linear approximation in tetrahedrons. Fields computed using GO and CGO are compared to results from the electromagnetic wave solver *LPSE*. Excellent agreement is obtained in 1-D linear and nonlinear permittivity profiles. Good agreement is also obtained for ICF-like Gaussian density profiles in 2-D. Finally, we demonstrate how the model reproduces Gaussian beam diffraction using CGO. The *IFRIIT* code will be interfaced inline to 3-D radiative hydrodynamic codes to describe the nonlinear laser plasma interaction in ICF and high-energy-density plasmas.

I. INTRODUCTION

High Energy Density (HED) plasmas created by laser matter interaction are prone to a variety of Laser Plasma Instabilities (LPI). In certain regimes, notably in the case of Inertial Confinement Fusion (ICF), these microscopic-scale processes may induce macroscopic-scale perturbations[1–3]. Notably, overlapping laser beams may exchange energy by coupling locally to ion acoustic waves, thereby redistributing the laser energy on large spatial scales[4–6]. Additionally, processes that excite electron plasma waves, such as two-plasmon decay or stimulated Raman scattering, can generate suprathermal electron populations that may modify the physics of shock propagation in nefarious or beneficial ways[7–9], or preheat the fuel during its compression[3]. While these processes are paramount to understanding and designing experiments, it is challenging to account for their contributions in hydrodynamic codes. In particular, we mention that for ICF applications, Cross-Beam Energy Transfer (CBET) is the first process that should be accounted for accurately because it redistributes laser energy on large scales, which modifies other LPI processes.

Modeling LPIs inline in hydrodynamic codes requires an efficient description of the laser propagation, e.g., ray-based approaches that retain the capability to estimate the laser intensity or field distribution in the plasma. In the vast majority of cases, laser models rely on conventional Geometrical Optics (GO) to describe laser refraction and collisional absorption[10]. GO rays are discrete trajectories in space, without notion of thickness, which complicates the definition of ray intensity. This has motivated the development of many methods to compute inline ray intensities from ray powers: rigid-scale estimation from collisional absorption[11], neighboring ray trajectories as elementary cross sections[5,12], ray-path-length ratio to cell volumes as elementary cross sections[13], ray density field estimation[14] or Gaussian beamlets[15].

Conversely, the notion of ray amplitude exists, but the computation of ray fields requires one to find all rays that contribute to a given point and tracking their phase[16]. In theory, such a method allows for the exact resolution of the eikonal equation, that is the first-order term of the field amplitude expansion in inverse power of the wave number in the Helmholtz equation. Numerically accurate implementations however involve the use of Inverse Ray-Tracing (IRT) methods. This framework and its associated algorithms differ greatly from what is currently implemented in HED hydrodynamic codes, where light is traced forward from a lens in a medium whose dielectric properties are known on a hydrodynamic mesh. Reproducing typical ICF laser fields and CBET from the ray amplitude and phase was demonstrated recently in offline calculations, using 2-D interpolation methods to compute maps of ray phases and amplitudes[17] in place of IRT.

The computation of field distributions from the ray field in itself is a strong motivation for developing inline IRT methods; however, there are additional advan-

tages to using this class of algorithms. In standard inline models, hydrodynamic cells are used as a proxy to compute the laser matter coupling. This method belongs to the class of rigid-scale techniques, e.g., the hydrodynamic grid used to determine wavefield quantities has a fixed scale at a given time step, and does not adapt to gradients in laser-related quantities. This estimation method is straightforward to implement, but it possesses two main shortcomings that lead to unwanted side effects. First, rigid-scale estimation requires many rays in each cell in order to avoid noisy estimation or holes in the reconstructed quantities. This is difficult to ensure in 3-D and in regions where refraction is important, notably for the reflected wavefield in direct-drive geometries and glint in indirect-drive geometry. In both cases, these fields may interact through CBET with the incident laser beam and, as such, should be modeled with sufficient accuracy. Second, laser caustics, regions prone to nonlinear effects, are often largely under-resolved by hydrodynamic grids. This is because (i) caustics are seldom located in regions of interest for the plasma flow and (ii) they are only a few wavelengths thick. Even in instances where a mesh would be sufficiently refined to resolve a caustic region, one must address the question of divergence of the GO framework there. This is accounted for in some hydrocodes by imposing artificial limits on the maximum reconstructed intensity.

This work aims to tackle several of the aforementioned problems by implementing three novel components to an inline laser propagation model: IRT, real-valued and complex-valued Geometrical Optics (CGO) with Etalon Integrals (EI), and Adaptive Mesh Refinement (AMR). First, the question of ray statistics per cell, related to the correct estimation of forward and reflected wavefields, is addressed by the use of IRT. The IRT framework allows one to solve for the eikonal equation directly while also providing the opportunity to use both GO and CGO. The implementation of CGO allows one to model a wider range of beam propagation physics, such as refraction and absorption modification in strongly dissipative regions, higher field reconstruction accuracy at caustics, beam diffraction in the case of Gaussian beams written with a complex initial condition, and interaction with the cold plasma. The caustic field itself is obtained from the ray field using an EI method[18] that eliminates divergence. The last component is the implementation of a symmetric tetrahedron-based AMR algorithm within the IRT framework, which allows one to resolve laser caustics and sharp boundaries.

The model implementing these novel methods, *IFRIIT* (Inline Field Reconstruction and Interaction using Inverse Tracing), will be interfaced with various 3-D hydrodynamic codes in order to study ICF and HED physics in the presence of CBET and suprathermal electrons generated by laser plasma instabilities. The inline calculation, e.g. for CBET, would proceed as follows: (i) a laser mesh is built from constrained triangulation of the hydrodynamic inputs (only at initialization), (ii) IRT with either GO or CGO is used to compute fields at mesh vertices, using EIs at caustics and CBET gains from the previous timestep, (iii) CBET gains are recomputed at mesh vertices and fields are updated as required, (iv) the laser mesh is adaptively refined in regions of high gain gradients, fields and gains are recomputed as required, (v) energy deposition is calculated in each tetrahedron and summed over the hydrodynamic cells. This paper tackles the first two points, while the AMR step and CBET implementation will be presented in a follow up paper. Furthermore, this paper deals with propagation of scalar wavefields, i.e. *s*-polarized waves. The description of wavefield polarization and its rotation will be tackled in future work. In the long term, *IFRIIT* is planned to be shared as a community code.

The paper is organized as follows: in Sec. II, we present the implementation of an IRT algorithm in the framework of GO and CGO ray-tracing. The IRT model presented in Secs. II A and II B is formulated in the framework of a 3-D finite-element approach compatible with the usual inline modeling approaches and approximations. The propagation equations for CGO, as well as their implementation in a 3-D tetrahedral mesh are presented in Sec. II C. We then detail in Sec. III the EI method for field reconstruction at caustics. We notably present modifications to the standard uniform Airy asymptotics, which allows one to successfully apply the EI in dissipative media. Finally, in Sec. IV we present the application of *IFRIIT* to academic cases of GO and CGO propagation. These highlight the properties of CGO rays in various media and illustrate the accuracy of the modified EI for GO and CGO in simple configurations and ICF-like plasmas. Finally, our conclusions are presented in Sec. V.

II. FINITE ELEMENT REAL AND COMPLEX GEOMETRICAL OPTICS INVERSE RAY-TRACING

A. Inverse Ray-Tracing formulation

In this section, the formulation and implementation of IRT in the framework of GO and CGO are described.

1. Definition of ray parameters and caustics

Throughout the paper, we will refer to ray trajectories expressed with parametric equations of real valued or complex valued ray arguments (ζ_1, ζ_2, τ), noted as $\mathbf{r} = \mathbf{R}(\zeta_1, \zeta_2, \tau)$ for position and $\mathbf{p} = \mathbf{P}(\zeta_1, \zeta_2, \tau)$ for momentum. These parametric equations are specific to solving the eikonal equation (see Eq. (10)) using the method of characteristics, where we make use of three so-called *ray parameters*: (ζ_1, ζ_2, τ).

The first two parameters (ζ_1, ζ_2) describe the distribution of initial conditions for the ray on an initial surface $\mathbf{R}_0(\zeta_1, \zeta_2)$. Parameter τ is a propagation coordinate such

that the ray reaches a position noted $\mathbf{r}(\tau) = \mathbf{R}(\zeta_1, \zeta_2, \tau)$ at τ from initial coordinates $\mathbf{R}_0(\zeta_1, \zeta_2) = \mathbf{R}(\zeta_1, \zeta_2, 0)$. In the case of CGO, the ray parameters, initial surface function $\mathbf{R}_0$, and ray position function $\mathbf{R}$ are all complex valued.

The trajectory equations in Hamiltonian form define a mapping from the ray coordinate phase space (ζ_1, ζ_2, τ) to the configuration space (x, y, z). Throughout the paper, we will refer to *observation points* as real-space coordinates $(x', y', z') \in \mathbb{R}^3$, where we seek ray parameters such that $\mathbf{R}(\zeta_1, \zeta_2, \tau) = (x', y', z')$, i.e., complex ray trajectories that intersect real space. The prime symbol denotes the real part of a complex variable, or directly a real variable. In general, there can be several solutions to this problem, e.g., several different rays may reach the same observation point. Here we mention that rays can be qualified as *different* if their ray parameters differ sufficiently (see Sec. II A 2).

The parametric mapping from (ζ_1, ζ_2, τ) to (x, y, z) through $\mathbf{R}$ implies the use of a Jacobian for the coordinate transformation. This Jacobian may be non-invertible in some regions, which manifests itself by a local discontinuity in the number of rays in the mapping. This change in number of rays is referred to as a *caustic* or *catastrophe* in ray theory[19]. As shown in Sec. II C 4, the framework of GO and CGO near and at caustics breaks down, leading to infinite ray amplitudes. As will be shown in Sec. III, however, the ray parameters keep mathematical meaning and can be used to reconstruct the caustic field[16].

2. Implementation of Inverse Ray-Tracing for real valued and complex valued rays

IRT deals with finding all the ray parameters (ζ_1, ζ_2, τ) such that the end point of the corresponding rays is a desired observation point $\mathbf{r}_\mathrm{o} = (x_\mathrm{o}, y_\mathrm{o}, z_\mathrm{o})$. This problem can be seen as a minimization of the quantity $\|\mathbf{R}(\zeta_1, \zeta_2, \tau) - \mathbf{r}_\mathrm{o}\|_\infty$, where $\mathbf{R}$ is obtained by integrating the ray trajectory equations. Various algorithms have been tested to solve this optimization problem, including Broyden's method[20] and Krylov-subspace methods[21]. The best performance and accuracy have been found by employing a multi-dimensional exact Newton method with a line search algorithm. Here, we present a general overview of our implementation.

a. Initial guess. The starting point of a Newton iteration is a guess $\mathbf{u}_\mathrm{g} = (\zeta_1^\mathrm{g}, \zeta_2^\mathrm{g}, \tau^\mathrm{g})$, tracing a ray to $\mathbf{r}_\mathrm{g}$. For time-dependent calculations, an adequate guess is the solution values of (ζ_1, ζ_2, τ) obtained at a previous hydrodynamic timestep since, in general, hydrodynamic quantities evolve slowly. At initialization, initial guesses are obtained by direct tracing of GO rays in the mesh. This provides a mapping $\mathbf{G}$ from the 3-D phase space (ζ_1, ζ_2, τ) to the physical space, $\mathbf{G} : (\zeta_1, \zeta_2, \tau) \to (x, y, z)$, where $\zeta_1 \in [\zeta_1^\mathrm{min}, \zeta_1^\mathrm{max}], \zeta_2 \in [\zeta_2^\mathrm{min}, \zeta_2^\mathrm{max}], \tau \in [\tau^\mathrm{min}, \tau^\mathrm{max}]$ are constrained by limits that depend on the configuration. For each observation point $\mathbf{r}_\mathrm{o}$, we identify local minima in $\|\mathbf{G} - \mathbf{r}_\mathrm{o}\|_\mathrm{L2}$ by applying a 3-D minimum filter[22] with a 3x3x3 pixel mask, providing an arbitrary number of initial guesses n_g. A typical number of initial guesses for a single observation point is in the 5 to 20 range.

b. Newton iteration. For each initial guess, we conduct the full Newton iterations as follows:

- The Jacobian $\underline{\mathbf{J}}(\mathbf{u}_n)$ of $\mathbf{F}(\mathbf{u}_n) = \mathbf{R}(\mathbf{u}_n) - \mathbf{r}_\mathrm{o}$ is computed, where $\mathbf{u}_n$ is the ray parameter vector at Newton step n and the underline denotes a matrix quantity. We then solve $\underline{\mathbf{J}}(\mathbf{u}_n)\boldsymbol{\delta}_n = -\mathbf{F}(\mathbf{u}_n)$ for the gradient direction $\boldsymbol{\delta}_n$. Note that the Jacobian is evaluated at each Newton step for best convergence accuracy.

- A (α, β) Goldstein-Armijo line search algorithm determines the optimal step size K (Ref. 23) such that we obtain the new iterate $\mathbf{u}_{n+1} = \mathbf{u}_n + K\boldsymbol{\delta}_n$.

- Convergence is tested by applying stopping criteria on the nonlinear residual and the step length. The nonlinear residual criterion, which determines successful convergence, is written as $\|\mathbf{F}(\mathbf{u}_n)\|_\infty \leq 1\text{Å}$. While this may appear to be a strict convergence criterion, we have found that it is required to identify duplicate rays.

c. Duplicate removal. The Newton iterations reduce the n_g initial guesses to m_g solutions, e.g., rays that reach $\mathbf{r}_\mathrm{o}$. Among these, duplicates must be identified. Since two rays are unique if they differ in ray parameters, rays i and j are supposedly different if $|\mu_i - \mu_j| \geq 10^{-3}\,[1 + \max(|\mu_i|, |\mu_j|)]$ μm where $\mu \equiv (\zeta_1, \zeta_2, \tau)$ (in microns). This criterion has been applied for 3ω laser light, and may need to be scaled for other frequencies. Usually, $n_\mathrm{s} = 2$ solutions remain in configurations of a simple fold caustic. The procedure is repeated for each observation point.

d. Jacobian evaluations. The Jacobian of $\mathbf{F}(\mathbf{u}_n)$ cannot be represented symbolically and must be approximated. Convergence performance of the Newton step has been observed to depend greatly on the spatial smoothness of the Jacobian function. As such, Krylov-subspace approximations of the Jacobian have been found to be inefficient for our purpose[36], which motivated our use of an exact Newton method. In most cases, the initial guesses are close to the actual solutions. In these conditions, central difference approximations have been found to lead to faster convergence rates than forward differences. The jacobians for GO and CGO read:

$$\underline{\mathbf{J}}_{\mathrm{GO}} = \begin{pmatrix} \frac{\partial R_x}{\partial \zeta_1} & \frac{\partial R_x}{\partial \zeta_2} & p_x \\ \frac{\partial R_y}{\partial \zeta_1} & \frac{\partial R_y}{\partial \zeta_2} & p_y \\ \frac{\partial R_z}{\partial \zeta_1} & \frac{\partial R_z}{\partial \zeta_2} & p_z \end{pmatrix} ,$$

$$\underline{\mathbf{J}}_{\mathrm{CGO}} = \begin{pmatrix} \frac{\partial R'_x}{\partial \zeta'_1} & \frac{\partial R'_x}{\partial \zeta'_2} & \frac{\partial R'_x}{\partial \tau'} & \frac{\partial R'_x}{\partial \zeta''_1} & \frac{\partial R'_x}{\partial \zeta''_2} & \frac{\partial R'_x}{\partial \tau''} \\ \frac{\partial R'_y}{\partial \zeta'_1} & \frac{\partial R'_y}{\partial \zeta'_2} & \frac{\partial R'_y}{\partial \tau'} & \frac{\partial R'_y}{\partial \zeta''_1} & \frac{\partial R'_y}{\partial \zeta''_2} & \frac{\partial R'_y}{\partial \tau''} \\ \cdots & & & & & \\ \frac{\partial R''_z}{\partial \zeta'_1} & \frac{\partial R''_z}{\partial \zeta'_2} & \frac{\partial R''_z}{\partial \tau'} & \frac{\partial R''_z}{\partial \zeta''_1} & \frac{\partial R''_z}{\partial \zeta''_2} & \frac{\partial R''_z}{\partial \tau''} \end{pmatrix} , \quad (1)$$

where we have defined $\mathbf{R}(\mathbf{u}_n) = (R_x, R_y, R_z)$ for GO and $\mathbf{R}(\mathbf{u}_n) = (R'_x, R'_y, R'_z, R''_x, R''_y, R''_z)$ for CGO, and have used $\partial\mathbf{R}/\partial\tau = \mathbf{p} = (p_x, p_y, p_z)$ for GO. Here and throughout the paper, the double prime denotes the imaginary part (and we recall that the single prime denotes the real part).

Evaluation of $\underline{\mathbf{J}}_{\mathrm{GO}}$ requires tracing 5 rays since the last column is known from one ray only. In the CGO case, 12 rays are required. Derivatives are evaluated with a central difference formula, with steps $\mathrm{d}\sigma^i = U^{1/3}\max(1, |u_n^i|)$ μm, where U is the machine precision (dimensionless) and u_n^i (in microns) is the i^{th} element of the Newton function vector $\mathbf{u}_n = (\zeta_1, \zeta_2, \tau)$ for GO and $\mathbf{u}_n = (\zeta'_1, \zeta'_2, \tau', \zeta''_1, \zeta''_2, \tau'')$ for CGO.

e. Trajectories and amplitudes. The Newton step is conducted on ray trajectories without integration of the phase and amplitude equations. Consequently, all rays converging to an observation point are found, including depleted and low-amplitude rays. This approach is efficient because the amplitude and phase integration is costly. Retaining low-amplitude rays is also advantageous for accurate CBET computations since these rays may have otherwise been neglected. After obtaining the n_s solutions for a given observation point, the fields are computed by integrating the phase and amplitude equations along the solution rays (see Sec. II C).

The exact Newton solver implemented in *IFRIIT* is based on the *SUNDIALS* libraries[25].

B. Mesh configuration

The GO and CGO trajectories in *IFRIIT* are resolved within an independent mesh that describes the hydrodynamic quantities and the dielectric permittivity ϵ of the medium. This section details the 3-D mesh configuration and its integration in the IRT framework.

1. Spatial tesselation of input points

The dielectric permittivity of the medium in 3-D is represented by a piecewise linear function. This simple approximation retains model efficiency since the formulation aims at inline modeling and tracing of a large number of rays for the IRT framework. We make the distinction here between the *input points*, which may be vertices from a hydrodynamic mesh or a user-supplied point cloud, and the *laser mesh*, which is the mesh constructed in the model for the IRT step. Further references to the *mesh* or to *cells* alone refer to the laser mesh.

Each cell is chosen to be a tetrahedron, which enables one to make a unique determination of the subgrid gradient from the hydrodynamic quantities at vertices. The observation points of the IRT algorithm are chosen to be the cell vertices, which enables one to define subgrid variations of laser-based quantities such as fields and gain rates. This will facilitate the formulation of inline LPI models.

The mesh is a triangulation of the input points, taken here to be Delaunay at initialization. It relates point numbers to cells, and defines cell neighborhoods through faces and point neighborhoods with respect to the Delaunay distance. This triangulation may be constrained when the input points are from hydrodynamic calculations, thus ensuring that tetrahedrons belong only to one parent hydrodynamic cell. For time-dependent calculations, there is no need to update the triangulation as long as the topology of the hydrodynamic mesh is not modified, which is the case in most hydrodynamic codes (Euler, Lagrange and Arbitrary Lagrangian Eulerian approaches).

2. Bounding mesh for ray-entry calculations

The boundary of the simulation domain is formed by the convex hull of the initial triangulation; however, rays are defined on initial ray surfaces outside the simulation domain. Since the IRT framework involves tracing rays with different initial conditions at each Newton step (see Sec. II A 2), a large number of intersection calculations between the outside rays and the simulation domain boundary are required. A ray-entry calculation involves iteration over all external faces (i.e., faces of tetrahedrons on the convex hull of the simulation domain) to verify that the ray propagating in vacuum intersects inside a given face. Given the potentially large number of tetrahedrons that shares a face with the domain boundary, this approach is inefficient. As such, we implement a second, less refined mesh, to act as a ray-entry buffer. This mesh is referred to as *bounding mesh*.

The bounding mesh is a cube encompassing the simulation domain and typically composed of 30 points per face. Tetrahedrons in the bounding mesh connect to the convex hull of the simulation domain. An example of a simulation domain and bounding mesh is given in Fig. 1 in a simplified 2-D geometry. Since there are far fewer external faces in the bounding mesh, ray-entry calculations are greatly sped up. The medium in the bounding mesh is a vacuum, e.g., $\epsilon = 1$. Dielectric permittivity gradients are present in bounding mesh tetrahedrons that share a vertex with the simulation domain convex hull.

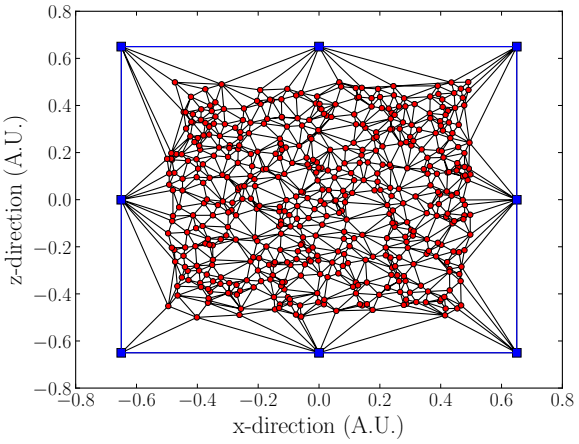

FIG. 1. Schematic illustration of the laser mesh in 2-D. Vertices belonging to the simulation domain are shown as red circles. Vertices belong to the bounding box are shown as blue squares. Black lines represent a Delaunay triangulation. External edges, used to calculate the ray entry, are shown as blue lines. Contrary to this simple example, the mesh used in *IFRIIT* is entirely 3-D.

These gradients are arbitrary and purely depend on how the bounding mesh is setup. Consequently, all gradients in the bounding mesh are manually set to zero, which creates discontinuities in ϵ at the boundary between the bounding mesh and the simulation domain, which are discussed in Sec. II C 8.

3. Subgrid scheme for hydrodynamic quantities

The triangulated mesh uniquely defines constant gradients in cells, such that the ray trajectories are of order 2 in space, e.g. ray coordinates can vary quadratically with arclength τ (see Sec. II C 3). This provides sufficient trajectory accuracy while retaining the performances required for inline modeling. Considering a quantity Λ known at vertices $i \in [1,4]$ of spatial coordinates $\mathbf{r}_i = (x_i, y_i, z_i) \in \mathbb{R}^3$ in a cell, we define the transformation matrix $\underline{\mathbf{A}}$:

$$\underline{\mathbf{A}} = \begin{pmatrix} x_2 - x_1 & x_3 - x_1 & x_4 - x_1 \\ y_2 - y_1 & y_3 - y_1 & y_4 - y_1 \\ z_2 - z_1 & z_3 - z_1 & z_4 - z_1 \end{pmatrix} , \tag{2}$$

where vertex 1 is chosen arbitrarily. This allows one to define a constant gradient $\mathcal{G}_\Lambda$ of quantity Λ within the tetrahedron from the values at the vertices:

$$\nabla\Lambda = \boldsymbol{\mathcal{G}}_\Lambda = (\underline{\mathbf{A}}^{-1})^T . \begin{pmatrix} \Lambda_2 - \Lambda_1 \\ \Lambda_3 - \Lambda_1 \\ \Lambda_4 - \Lambda_1 \end{pmatrix} . \tag{3}$$

The subgrid representation of Λ in the cell is then:

$$\Lambda(\mathbf{r}) = \Lambda_1 + (\mathrm{Re}(\mathbf{r}) - \mathbf{r}_1).\boldsymbol{\mathcal{G}}_\Lambda , \tag{4}$$

where $\mathbf{r}$ is a complex valued coordinate.

4. Subgrid scheme for the dielectric permittivity

As will be detailed in Sec. II C, the CGO framework does not make use of the $\epsilon'' \ll \epsilon'$ assumption. In order to derive the trajectory equations from the eikonal equation, the permittivity function must satisfy the Cauchy-Riemman equations, which prevents the use of the usual definition for ϵ (Eq. (4)). Consequently, the subgrid permittivity for CGO is written as:

$$\epsilon(\mathbf{r}) = \epsilon_1 + (\mathbf{r} - \mathbf{r}_1).\overline{\boldsymbol{\mathcal{G}}_\epsilon} , \tag{5}$$

where $\nabla\epsilon = \boldsymbol{\mathcal{G}}_\epsilon$ is a constant in each cell, and the overline denotes complex conjugation. Throughout the paper, the dot product involving complex quantities is defined as $a.b = \sum a_i \overline{b_i}$. Decomposing the dielectric permittivity into real and imaginary parts yields:

$$\epsilon'(\mathbf{r}' + \imath\mathbf{r}'') = \epsilon'_1 + (\mathbf{r}' - \mathbf{r}_1).\boldsymbol{\mathcal{G}}'_\epsilon - \mathbf{r}''.\boldsymbol{\mathcal{G}}''_\epsilon , \tag{6}$$

$$\epsilon''(\mathbf{r}' + \imath\mathbf{r}'') = \epsilon''_1 + (\mathbf{r}' - \mathbf{r}_1).\boldsymbol{\mathcal{G}}''_\epsilon + \mathbf{r}''.\boldsymbol{\mathcal{G}}'_\epsilon . \tag{7}$$

In real valued GO ($\mathbf{r}'' = 0$), ϵ' is a function of $\boldsymbol{\mathcal{G}}'_\epsilon$ and ϵ'' is a function of $\boldsymbol{\mathcal{G}}''_\epsilon$. These equations illustrate how this no longer holds in CGO, where the ray position in complex space modifies the real part of the permittivity seen by the ray through $\boldsymbol{\mathcal{G}}''_\epsilon$ and vice versa.

The trajectory equations for GO and CGO rays are solved in each tetrahedron separately using the assumption that $\boldsymbol{\mathcal{G}}_\epsilon$ is locally constant. When reaching a cell interface, the neighbor tetrahedron is determined from topology and the integration is continued in the next tetrahedron.

C. Propagation equations for real and complex rays

We now present the propagation equations of GO and CGO along with their implementation in *IFRIIT*. Some derivations are only given for CGO and are straightforward to simplify for GO. First, we derive the eikonal and transport equations in Sec. II C 1, required to describe the ray trajectory, phase, and field equations given for GO in Sec. II C 2 and CGO in Sec. II C 3. Computation of the ray amplitude term, uniquely dependent on the ray trajectory, is given for both GO and CGO in Sec. II C 4. The CGO ray trajectory equation in a linear permittivity profile is derived in Sec. II C 5, and the corresponding integrations for complex arc-length and complex phase are given in Secs. II C 6 and II C 7, respectively. Transition of

the ray from one tetrahedron to the next involves a complex momentum discontinuity, expressed in Sec. II C 8. Finally, initialization of complex momentum for CGO is given in Sec. II C 9.

1. Eikonal and transport equation

Both the GO and CGO formalisms deal with solutions of the Helmholtz equation, obtained from the Maxwell equations for monochromatic *s*-polarized electromagnetic waves[26]:

$$\Delta u(\mathbf{r}) + k_0^2 \epsilon(\mathbf{r}) u(\mathbf{r}) = 0 \ , \tag{8}$$

where $k_0 = \omega_0/c$ is the vacuum wave number and u is the scalar electric field.

The eikonal and transport equations are obtained by performing a Debye expansion:

$$u(\mathbf{r}) = \sum_m \frac{A_m(\mathbf{r})}{(\imath k_0)^m} \exp\left[\imath k_0 \psi(\mathbf{r})\right] \ , \tag{9}$$

where ψ is a phase and A_m an amplitude. In the most generic description, the phase and amplitude terms may be complex-valued. Note also that with these notations, the phase has units of distance and the amplitude term A_m has units of u times an inverse distance to the power m (such that A_0 has units of u).

Substitution of this ansatz in the Helmholtz equation and equating terms in inverse powers of $(\imath k_0)^m$ leads, at order 0, to the eikonal equation:

$$(\nabla\psi)^2 = \epsilon(\mathbf{r}) \ , \tag{10}$$

and at order 1, to the first transport equation:

$$2(\nabla A_0 . \nabla\psi) + A_0 \Delta\psi = 0 \ . \tag{11}$$

The eikonal equation belongs to the Hamilton-Jacobi variety and is, in general, solved using the method of characteristics to obtain the trajectory equations in *Hamiltonian form*[16]. Note here that we have assumed *s*-polarized light. An extension of the model to more generic polarization configurations is envisioned as follows: Away from turning points, Eq. (8) can be used to propagate the *p*-polarized component. Doing so, the electric field vector can be tracked in a local ray-centered coordinate system such as the one employed in Paraxial Complex Geometrical Optics[15]. This would allow for more accurate computation of LPI processes and eventually account for polarization rotation due to CBET.

2. Geometrical Optics ray trajectory, phase, and field

One of the differences between GO and CGO arises in the expression of the dielectric permittivity $\epsilon(\mathbf{r}) = \epsilon'(\mathbf{r}) + \imath\epsilon''(\mathbf{r})$. In GO, ray trajectories are localized in real space, which requires the assumption $\epsilon''(\mathbf{r}) \ll \epsilon'(\mathbf{r})$. In that case, solutions to the eikonal equation are sought in the form of $\psi(\mathbf{r}) = \psi^{(0)}(\mathbf{r}) + \psi^{(1)}(\mathbf{r})$, where $\psi^{(0)}(\mathbf{r})$ is real valued, $\psi^{(1)}(\mathbf{r})$ is imaginary, and $|\psi^{(1)}| \ll |\psi^{(0)}|$. Substituting the phase ansatz into the eikonal equation (10) and equating terms of the same order yields:

$$(\nabla\psi^{(0)})^2 = \epsilon'(\mathbf{r}) \ , \tag{12}$$

$$2\nabla\psi^{(0)} . \nabla\psi^{(1)} = \imath\epsilon''(\mathbf{r}) \ , \tag{13}$$

$$(\nabla\psi^{(1)})^2 = 0 \ . \tag{14}$$

Solving Eq. (12) using the method of characteristics yields the real-space GO trajectory and phase equations[16]:

$$\frac{\mathrm{d}\mathbf{r}'}{\mathrm{d}\tau'} = \mathbf{p}' \ , \tag{15}$$

$$\frac{\mathrm{d}\mathbf{p}'}{\mathrm{d}\tau'} = \frac{1}{2}\nabla\epsilon'(\mathbf{r}') \ , \tag{16}$$

$$\frac{\mathrm{d}\psi^{(0)}}{\mathrm{d}\tau'} = \epsilon'(\mathbf{r}') \ , \tag{17}$$

where $\mathbf{p}' = \nabla\psi^{(0)}$ is the real ray momentum.

Using the unperturbed ray momentum $\nabla\psi^{(0)} = \frac{\mathrm{d}\mathbf{r}'}{\mathrm{d}\tau'}$, Eq. (13) becomes $\mathrm{d}\psi^{(1)}/\mathrm{d}\tau' = \imath\epsilon''/2$, which can be integrated to give the phase correction term:

$$\psi^{(1)} = \frac{1}{2}\int_0^{\tau'} \imath\epsilon''(\mathbf{r}'(\tilde{\tau}'))\mathrm{d}\tilde{\tau}' \ . \tag{18}$$

Finally, the GO electric-field amplitude is[16]:

$$|u|_{\mathrm{GO}} = |A_0(\tau')| \exp\left(-k_0 \frac{1}{2}\int_0^{\tau'} \epsilon''(\mathbf{r}'(\tilde{\tau}'))\mathrm{d}\tilde{\tau}'\right) \ . \tag{19}$$

In the case of plasmas, the quantity in the exponential is the well-known Inverse Bremsstrahlung absorption term (and eventually CBET amplification term) used in GO-based ray-tracing codes. The ray amplitude term $|A_0(\tau')|$ accounts for local field amplification through convergence/divergence of the ray tube and is discussed further in Sec. II C 4.

3. Complex Geometrical Optics ray trajectory, phase, and field

In the CGO framework, no assumption is made on the amplitude of ϵ''. The eikonal and transport equations (Eqs. (10) and (11)) are solved by seeking complex valued ray phases, momenta, and positions. The CGO trajectory and phase equations are:

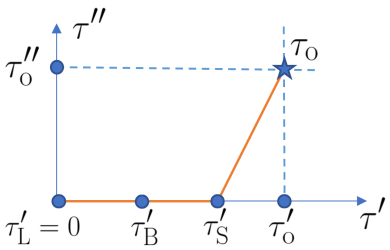

FIG. 2. Integration path chosen for the CGO IRT. Rays are propagating from the lens plane (at $\tau = 0$) to the bounding mesh boundary ($\tau'_{\rm B}$) and simulation box boundary ($\tau'_{\rm S}$) along the real axis. This first part of the contour minimizes ray shift into complex space, which facilitates convergence of the IRT algorithms. The jump conditions between vacuum and the boundary of the simulation mesh is applied at $\tau'_{\rm S}$. Integration is then carried along a straight line of slope $\alpha = \tau''_{\rm o}/(\tau'_{\rm o} - \tau'_S)$ to $\tau_{\rm o}$.

$$\frac{\mathrm{d}\mathbf{r}}{\mathrm{d}\tau} = \mathbf{p} \ , \tag{20}$$

$$\frac{\mathrm{d}\mathbf{p}}{\mathrm{d}\tau} = \frac{1}{2}\nabla\epsilon(\mathbf{r}) \ , \tag{21}$$

$$\frac{\mathrm{d}\psi}{\mathrm{d}\tau} = \epsilon(\mathbf{r}) \ ,$$

where the ray parameter τ is also complex valued.

Integration of these equations against the complex parameter requires a choice of path in complex space. Since the subgrid representation of $\epsilon(\mathbf{r})$ satisfies the Cauchy-Riemman equations in each cell, any choice of a path for τ will lead to identical results, within numerical precision. In terms of numerical implementation, we have found that a straight-line integration in the simulation domain minimizes trajectory errors and is more straightforward to formulate. The integration path is shown in Fig. 2.

4. Determination of ray amplitude

The ray amplitude term A_0 is the solution of the first-order transport equation (Eq. (11)). It can be reduced to an ordinary differential equation in τ by using the ray trajectory equations:

$$2\frac{\mathrm{d}A_0}{\mathrm{d}\tau} + A_0\Delta\psi = 0 \ , \tag{22}$$

where we have used $\nabla\psi = \mathbf{p}$ and $\nabla A_0.\mathbf{p} = \mathrm{d}A_0/\mathrm{d}\tau$. Integration against the arc-length yields:

$$A_0(\tau) = A_0^0 \exp\left(-\frac{1}{2}\int_0^\tau \Delta\psi(\tilde{\tau})\mathrm{d}\tilde{\tau}\right) \ , \tag{23}$$

with A_0^0 the initial ray amplitude at $\tau = 0$. This equation can be further simplified by noting that $\Delta\psi = \nabla.\mathbf{p}$ and $\nabla.\mathbf{p} = \mathrm{d}\ln D(\tau)/\mathrm{d}\tau$, where $D(\tau)$ is the determinant of the Jacobian of the transformation from the spatial coordinates (x, y, z) to the ray coordinates (ζ_1, ζ_2, τ):

$$D(\tau) = \left(\frac{\partial\mathbf{r}}{\partial\zeta_1} \times \frac{\partial\mathbf{r}}{\partial\zeta_2}\right).\mathbf{p} \ , \tag{24}$$

where we have used $\partial\mathbf{r}/\partial\tau = \mathbf{p}$. Substituting for Eq. (24) in Eq. (23) and integrating yields the equation for the ray amplitude[16]:

$$A_0(\tau) = A_0^0\left(\frac{D_0}{D(\tau)}\right)^{1/2} \ , \tag{25}$$

where $D_0 = D(0)$ is the initial ray divergence. Note that in GO, the Jacobian determinant D is real valued, while in CGO the derivatives in Eq. (24) must be taken with respect to complex variable $\mathbf{r}$ and complex arguments ζ. As such, the square root in Eq. (25) possesses two branches in CGO. In the presence of a caustic, the phase of the reflected wavefield must be shifted by $-\pi/2$. This shift justifies a root selection for the two branches of $\sqrt{D(\tau)}$ such that the phase of the reflected ray is shifted by $-\pi/2$ compared to that of the incoming ray.

Equation (25) expresses the conservation of energy in a ray tube formed by a ray bundle of infinitely small cross section. As such, it expresses the contribution of refraction to the ray amplitude, i.e., the focusing or divergence of the field in density gradients and at discrete interfaces. This term becomes unity when integrating on an elementary cross section, which yields the conventional definition of ray power used in GO ray-tracing codes. It remains important however for the purpose of electric field computation.

5. Trajectory equation in linear dielectric permittivity profile

The trajectory equations (20) can be integrated analytically for a medium with constant permittivity gradient $\boldsymbol{\mathcal{G}}_\epsilon$:

$$\mathbf{r}(\tau) = \mathbf{r}_0 + \mathbf{p}_0\tau + \frac{\tau^2}{4}\boldsymbol{\mathcal{G}}_\epsilon \ , \tag{26}$$

$$\mathbf{p}(\tau) = \mathbf{p}_0 + \frac{\tau}{2}\boldsymbol{\mathcal{G}}_\epsilon \ , \tag{27}$$

where $\mathbf{r}_0 \equiv \mathbf{r}(0)$ and $\mathbf{p}_0 \equiv \mathbf{p}(0)$.

Let us consider a complex ray traced from $\tau = 0$ to $\tau = \tau'(1 + \imath\alpha)$, where here $\alpha = \tau''/\tau'$. The real and imaginary parts of the trajectory equations are:

$$\mathbf{r}'(\tau) = \mathbf{r}'_0 + \tau'(\mathbf{p}'_0 - \alpha\mathbf{p}''_0) + \frac{\tau'^2}{4}\left[(1-\alpha^2)\boldsymbol{\mathcal{G}}'_\epsilon - 2\alpha\boldsymbol{\mathcal{G}}''_\epsilon\right] ,$$
$$\mathbf{r}''(\tau) = \mathbf{r}''_0 + \tau'(\mathbf{p}'_0\alpha + \mathbf{p}''_0) + \frac{\tau'^2}{4}\left[(1-\alpha^2)\boldsymbol{\mathcal{G}}''_\epsilon + 2\alpha\boldsymbol{\mathcal{G}}'_\epsilon\right] ,$$
$$\mathbf{p}'(\tau) = \mathbf{p}'_0 + \frac{\tau'}{2}(\boldsymbol{\mathcal{G}}'_\epsilon - \alpha\boldsymbol{\mathcal{G}}''_\epsilon) ,$$
$$\mathbf{p}''(\tau) = \mathbf{p}''_0 + \frac{\tau'}{2}(\boldsymbol{\mathcal{G}}''_\epsilon + \alpha\boldsymbol{\mathcal{G}}'_\epsilon) . \quad (28)$$

These separated trajectory equations are useful for illustrating how complex rays propagate. We recall that complex rays have physical meaning only when they intersect real space, e.g., for $\mathbf{r}''(\tau) = 0$. In general, the initial complex momentum $\mathbf{p}''_0$ is non zero, and relates to the initial phase (see Sec. II C 9). The inital complex position $\mathbf{r}''_0$ depends on the complex valued ray parameters (ζ_1, ζ_2) obtained by the IRT. We highlight a few properties of complex rays that can be observed from Eq. (28):

- CGO rays propagate with $\alpha = 0$ only in the lit side (e.g., in front of caustics) of media with $\epsilon'' = 0$.
- CGO rays with real valued initial position and momentum shift into complex space when $\alpha \neq 0$. This is the case even in constant density media since the vacuum/plasma interface is a discontinuity in ϵ that shifts ray momentum in complex space (see Sec. II C 8).
- Ray position is affected by $\boldsymbol{\mathcal{G}}''_\epsilon$, implying that ϵ'' gradients (e.g., from Inverse Bremsstrahlung collision frequencies or CBET gain rates) shift ray positions.
- A CGO ray in vacuum may be complex valued if its initial condition is also complex, as is the case for, e.g., a Gaussian beam (see Sec. IV C).

6. Equation integration in tetrahedrons

Propagation of a GO or CGO ray within a tetrahedron involves determining (i) the arc-length τ_c at which the ray exits the cell, and (ii) the corresponding exit face. For a given Newton step, the slope parameter $\alpha = \tau''/\tau'$ is fixed. As such, the only unknown in Eqs. (28) is τ'_c. Since the tetrahedron boundaries are known in physical space, inversion of the ray equations to find τ'_c is conducted on the real part of the ray trajectory $\mathbf{r}'$. In general, this equation is second order in τ', so that there are at most two solutions per face, corresponding to eight solutions for a given tetrahedron. Selection of the solution then follows Fermat's principle: the correct solution provides a minimum strictly positive travel time[27].

Resolution of the ray trajectory equation is conducted in a non-Cartesian local coordinate system where the three spatial axes are three arbitrary edges of the tetrahedron. We define the ray position $\hat{\mathbf{r}} = (\hat{x}, \hat{y}, \hat{z})$, momentum $\hat{\mathbf{p}}$, and gradient $\hat{\boldsymbol{\mathcal{G}}}_\epsilon$ in the local coordinate system as:

$$\hat{\mathbf{r}} = \underline{\mathbf{A}}^{-1}\mathbf{r} \ , \ \hat{\mathbf{p}} = \underline{\mathbf{A}}^{-1}\mathbf{p} \ , \ \hat{\boldsymbol{\mathcal{G}}}_\epsilon = \underline{\mathbf{A}}^{-1}\boldsymbol{\mathcal{G}}_\epsilon , \quad (29)$$

where $\underline{\mathbf{A}}$ is the matrix defined in Eq. (2).

In this coordinate system, $\{\hat{x}' = 0, \forall(\hat{y}', \hat{z}') \in [0,1]\}$ is the face formed by nodes (2,3,4), $\{\hat{y}' = 0, \forall(\hat{x}', \hat{z}') \in [0,1]\}$ is the face formed by nodes (1,3,4), $\{\hat{z}' = 0, \forall(\hat{x}', \hat{y}') \in [0,1]\}$ is the face formed by nodes (1,2,4), and $\{\forall(\hat{x}', \hat{y}', \hat{z}')\backslash\ \hat{x}' + \hat{y}' + \hat{z}' = 1\}$ is the face formed by nodes (1,2,3). Multiplying both sides of Eq. (28) by $\underline{\mathbf{A}}^{-1}$ gives:

$$\hat{\mathbf{r}}'(\tau) = \hat{\mathbf{r}}'_0 + \tau'(\hat{\mathbf{p}}'_0 - \alpha\hat{\mathbf{p}}''_0) + \frac{\tau'^2}{4}\left((1-\alpha^2)\hat{\boldsymbol{\mathcal{G}}}'_\epsilon - 2\alpha\hat{\boldsymbol{\mathcal{G}}}''_\epsilon\right) . \quad (30)$$

The eight intersection solutions are obtained by solving for $\hat{x}'(\tau) = 0$, $\hat{y}'(\tau) = 0$, $\hat{z}'(\tau) = 0$, and $\hat{x}'(\tau) + \hat{y}'(\tau) + \hat{z}'(\tau) = 1$. Numerical precision issues can lead to erroneous solutions for τ' when it is comparable to machine precision, or when a ray's turning point is too close to a face. We have found it necessary to impose the additional constraint that the real-space coordinate must be outside of the output face at coordinate $\tau' + \mathrm{d}\tau'$, where $\mathrm{d}\tau'$ is an infinitesimal arc-length.

Once a solution for τ' is found, the complex ray momentum and position can be updated by substituting for the solution τ' in Eqs. (28). Using the neighborhood information of the mesh, the ray is then propagated in the next tetrahedron from the previous output face.

Resolution of the ray equation in the local coordinate system provides control over the precision, notably when rays are directly incident on vertices. In that case, various algorithms are applied to displace rays slightly inside the face before computing the arc-length. It must be noted that reliability of the propagation algorithm in IRT is paramount since ray trajectories are used to compute Jacobian functions, which in turn are used to find the rays reaching observation points.

7. Phase equation in tetrahedrons

Once the solution for τ has been found in a tetrahedron, the phase change can be computed analytically by integrating ϵ along the complex ray trajectory:

$$\psi_\tau - \psi_0 = \int_0^\tau \epsilon\left[\mathbf{r}(\tau)\right] \mathrm{d}\tau \ , \quad (31)$$

where ψ_0 is the phase at the initial ray position in the cell. Substituting the sub-grid description of ϵ from Eq. (5) and using the expression of $\mathbf{r}(\tau)$ from Eq. (26), we obtain:

$$\psi_\tau - \psi_0 = \tau \left[\epsilon_0 + \frac{\tau}{2} \left(\mathbf{p}_0 + \frac{\boldsymbol{\mathcal{G}}_\epsilon \tau}{6} \right) . \overline{\boldsymbol{\mathcal{G}}_\epsilon} \right] , \qquad (32)$$

where we have used $\epsilon_0 = \epsilon_1 + (\mathbf{r}_0 - \mathbf{r}_1).\overline{\boldsymbol{\mathcal{G}}_\epsilon}$, with $\epsilon_0 \equiv \epsilon(\tau = 0)$ the dielectric permittivity at the initial ray position, $\mathbf{r}_1$ the real-space coordinate of node 1 of the current tetrahedron, and ϵ_1 the corresponding permittivity.

8. Complex ray refraction at permittivity discontinuities

It is well known that light rays experience momentum changes at discrete interfaces. The piecewise linear dielectric permittivity function assumed in *IFRIIT* is continuous in real space at interfaces, so that GO rays do not experience refraction at interfaces. In this section, we describe how this is not the case for CGO and show how the ray momentum is modified by discrete interfaces.

The permittivity jump from ϵ^{A} to ϵ^{B} between cells A and B at the interface point $\mathbf{r}_{\mathrm{AB}}$ is:

$$\epsilon^{\mathrm{B}} - \epsilon^{\mathrm{A}} = \mathbf{r}''_{\mathrm{AB}} . \left[\boldsymbol{\mathcal{G}}_\epsilon^{\prime\prime \mathrm{A}} - \boldsymbol{\mathcal{G}}_\epsilon^{\prime\prime \mathrm{B}} + \imath (\boldsymbol{\mathcal{G}}_\epsilon^{\prime \mathrm{B}} - \boldsymbol{\mathcal{G}}_\epsilon^{\prime \mathrm{A}}) \right] , \qquad (33)$$

where we have used Eq. (5) and the matching condition in physical space that derives from the construction of the gradients (see Eq. (3)). This equation shows that unless the ray is in physical space ($\mathbf{r}'' = 0$) or gradients in cells A and B are equal ($\boldsymbol{\mathcal{G}}_\epsilon^{\prime \mathrm{A}} = \boldsymbol{\mathcal{G}}_\epsilon^{\prime \mathrm{B}}$ and $\boldsymbol{\mathcal{G}}_\epsilon^{\prime\prime \mathrm{A}} = \boldsymbol{\mathcal{G}}_\epsilon^{\prime\prime \mathrm{B}}$), the permittivity is discontinuous in complex space even though it is continuous in real space.

We now derive the jump conditions involved with a complex ray traversing a face with a localized permittivity jump. These are obtained by solving the complex ray equation (20) in a linear permittivity layer, expressing the output position and momentum of the ray as a function of the layer thickness. By taking the layer thickness to be zero, we obtain a discrete permittivity jump and the related momentum jump equations. Consider a ray at initial position $\mathbf{r}_0$ and momentum $\mathbf{p}_0$ on the face of the tetrahedron it is leaving. The face normal is noted $\mathbf{q}$ and is assumed to be outward with respect to the tetrahedron. The ray is traveling to position $\mathbf{r}_1$ in the input face of the tetrahedron into which it is entering, such that $\mathbf{r}_1 = \mathbf{r}_0 + L\mathbf{q}$ (with $L \to 0$). The dielectric permittivity is assumed to vary linearly along the face normal: $\epsilon(\mathbf{r}) = \epsilon_0 + (\mathbf{r} - \mathbf{r}_0).\mathbf{q}(\epsilon_1 - \epsilon_0)/L$.

The complex ray trajectory equation at $\mathbf{r}'(\tau_1) = \mathbf{r}_1$, projected along the face normal, is:

$$-L + \tau_1 \mathbf{p}.\mathbf{q} - \frac{\tau_1^2}{4L}(\epsilon_1 - \epsilon_0) = 0 , \qquad (34)$$

where we have used $\mathbf{q}.\mathbf{q} = 1$. Solving this equation for τ_1 yields:

$$\tau_1 = -2L[\mathbf{p}_0.\mathbf{q} \pm \sqrt{(\mathbf{p}_0.\mathbf{q})^2 + (\epsilon_1 - \epsilon_0)}]/(\epsilon_1 - \epsilon_0) , \qquad (35)$$

$$\mathbf{p}_1 = \mathbf{p}_0 + [-\mathbf{p}_0.\mathbf{q} \pm \sqrt{(\mathbf{p}_0.\mathbf{q})^2 + (\epsilon_1 - \epsilon_0)}]\mathbf{q} . \qquad (36)$$

We select the root corresponding to minimum travel time $|\tau_1/L|$ to compute the momentum after the permittivity jump $\mathbf{p}_1$.

Equation (36) highlights a unique feature of CGO: rays are never reflected at discrete interfaces, as opposed to GO rays which would reflect for $\mathbf{p}'_0.\mathbf{q} + (\epsilon'_1 - \epsilon'_0) < 0$ with $\mathbf{p}_1 = \mathbf{p}_0 - 2(\mathbf{q}.\mathbf{p}_0)\mathbf{q}$. Instead, the CGO solution behind such an interface would be exponentially damped. When all quantities are real valued, the jump conditions (Eq. (36)) are equivalent to Snell refraction of monochromatic light. In the CGO case, the rays also shift in complex momentum space. These equations are implemented at (i) the interface between the bounding-box vacuum and the material mesh, where $\epsilon_0 = 1$, and (ii) every tetrahedron interface when $\mathbf{r}'' \neq 0$, which is the case when computing the CGO ray amplitude.

9. Complex initial conditions

Initial positions of GO and CGO rays are defined on the initial ray surface through the function $\mathbf{R}_0$. Ray phases and amplitudes are also defined on the initial ray surface through corresponding functions ψ_0 and A_0^0:

$$\mathbf{R}(\zeta_1, \zeta_2, 0) = \mathbf{R}_0(\zeta_1, \zeta_2) , \qquad (37)$$

$$\psi(\zeta_1, \zeta_2, 0) = \psi_0(\zeta_1, \zeta_2) , \qquad (38)$$

$$A_0(\zeta_1, \zeta_2, 0) = A_0^0(\zeta_1, \zeta_2) , \qquad (39)$$

where the initial functions depend on the ray parameters. A simple ansatz of the complex initial ray position function is $\mathbf{R}_0(\zeta_1, \zeta_2) = \mathbf{r}_{\mathrm{lens}} + \mathbf{e}_1\zeta_1 + \mathbf{e}_2\zeta_2$, with $\mathbf{r}_{\mathrm{lens}} \in \mathbb{R}^3$ a lens position and $\mathbf{e}_i \in \mathbb{R}^3$ two orthogonal base vectors in the lens plane. The initial phase function for a plane-wave is then $\psi_0(\zeta_1, \zeta_2) = 0$ whatever the actual angle of the beam. For an initially circular Gaussian beam, as considered in Sec. IV C, the initial phase function reads $\psi_0(\zeta_1, \zeta_2) = \imath(\zeta_1^2 + \zeta_2^2)/(2k_0 w_0^2)$ with w_0 an initial radius.

The initial momentum $\mathbf{p}_0$ of the rays can be obtained by differentiating Eq. (38) and from the eikonal equation on the initial curve:

$$\mathbf{p}_0 . \frac{\partial \mathbf{R}_0}{\partial \zeta_1} = \frac{\partial \psi_0}{\partial \zeta_1} , \qquad (40)$$

$$\mathbf{p}_0 . \frac{\partial \mathbf{R}_0}{\partial \zeta_2} = \frac{\partial \psi_0}{\partial \zeta_2} , \qquad (41)$$

$$\mathbf{p}_0 . \mathbf{p}_0 = \epsilon^0 = 1 , \qquad (42)$$

where the rays are assumed to be initialized in vacuum, e.g., $\epsilon^0 = 1$. These equations illustrate that the initial momentum is real valued unless the right-hand side of Eq. (40) or Eq. (41) is complex valued, e.g, for Gaussian beams.

III. CALCULATION OF CAUSTIC FIELDS USING ETALON INTEGRALS

Caustics are singularities in the mapping from the ray coordinate phase space to the configuration space, which manifest as a degeneracy in the number of rays reaching a given observation point. Mathematically, they correspond to non invertibility of the Jacobian $\mathbf{J}$, and hence to a divergence of the ray amplitude because $D(\tau) = 0$ in Eq. (25).

The Etalon Integral (EI) technique was developed to remedy this shortcoming of GO and CGO[18] and successfully applied in the case of a linear nondissipative permittivity profile in Ref. 28. This section details the implementation of the EI in the *IFRIIT* framework. Notably, we present modifications to the EI that are required for the successful application of the method to laser propagation in plasmas. The modifications are related to ray selection rules in the case of CGO in dissipative media and dissipation corrections for GO in dissipative media. In Sec. IV we will present applications of the method to nonlinear permittivity profiles using both GO and CGO.

A. Validity of the GO and CGO framework

The formalism of GO and CGO breaks down not only at the divergence point itself, where $D(\tau) = 0$, but also in a small volume around the caustic called the *caustic zone*. The volume of the caustic zone can be estimated from the validity conditions of GO and CGO. One such condition is that the phase and amplitude of rays must not vary significantly over the *Fresnel volume*, defined as a spatial volume essential to the field forming at a given point (see Ref. 29 for more details). A corollary of this condition is that the Fresnel volumes of adjacent rays should not overlap significantly. The latter can be expressed by requiring that the phase difference between two rays reaching the same observation point should be such that[29,30]:

$$|\psi_1 - \psi_2| \geq \lambda_0/2 \ . \tag{43}$$

This criterion is convenient for determining observation points where the GO and CGO methods will fail to produce a physical result. The region of inapplicability of the ray optics framework is a thin region of space on the lit side of the caustic for GO and on either side of the caustic for CGO. In practice, we have found that the ray solution remains valid up to $|\psi_1 - \psi_2| \geq \lambda_0/3$.

B. Etalon Integral

In regions of space where condition (43) is not met, we make use of an EI method[18] to reconstruct the electric field. The method is based on identifying standard integrals that match the electric field of various caustic types. In most ICF applications, caustics of the *fold* type are encountered. These are the simplest singularities and arise, e.g., in linear layers. A guess at the form of the caustic field is formulated such that deviations from the ideal case are allowed. Namely, the field near a fold-type caustic is approached by the sum of (i) an Airy function, analytical solution for the field in a constant density gradient, and (ii) the derivative of an Airy function, which can account, e.g., for weak caustic curvature or wavefront distortions[16]. This so-called *uniform Airy asymptotic* reads:

$$u(\mathbf{r}) \simeq \left\{ C_1(\mathbf{r})\tilde{I}[\xi(\mathbf{r})] - \imath C_2(\mathbf{r})\tilde{I}[\xi(\mathbf{r})]/k_0 \right\} \exp \imath k_0 \chi(\mathbf{r}) \ , \tag{44}$$

where $\tilde{I}(\xi) = k_0^{1/6}\sqrt{2\pi}\mathrm{Ai}(k_0^{2/3}\xi)$ is the dimensional Airy integral. Four functions of space $C_1(\mathbf{r}), C_2(\mathbf{r}), \chi(\mathbf{r})$ and $\xi(\mathbf{r})$ have been introduced in Eq. (44). Since the field given by the overlap of two rays also contains four parameters $(\psi_1, \psi_2, A_{01}, A_{02})$, the ray phases and amplitudes can be related to the uniform Airy asymptotic functions. By matching the fields asymptotically and equating the pre-exponential factors, the caustic field is then:

$$u = \sqrt{\pi}[(-\xi)^{1/4}(A_{01} + \imath A_{02})\mathrm{Ai}(\xi) - (-\xi)^{-1/4}(A_{02} + \imath A_{01})\mathrm{Ai}'(\xi)] \exp[\imath(k_0\chi - \pi/4)] \ , \tag{45}$$

where the ξ and χ parameters are related to the eikonal of the rays through:

$$\chi = \frac{1}{2}(\psi_1 + \psi_2) \ , \tag{46}$$

$$\xi = -\left(k_0 \frac{3}{4}(\psi_2 - \psi_1)\right)^{2/3} \ , \tag{47}$$

with subscripts 1 and 2 representing the two rays reaching the observation point, which must be ordered in a specific way to compute ξ correctly. Notably, the EI field must be oscillating in the lit side and decaying in the shadow side.

For a medium with $\epsilon'' = 0$, or for GO IRT, $\psi \in \mathbb{R}$ in the lit side and ψ is imaginary in the shadow side. In that case, the power function in Eq. (47) is bijective in the lit side with $\xi \in \mathbb{R}$, and there is a branch in the shadow side that gives $\xi \in \mathbb{R}$. The ray-ordering condition for applicability of the method for GO IRT reads:

$$\text{lit region :} \ \ \psi_1' < \psi_2' \ , \tag{48}$$

$$\text{shadow region :} \ \ \psi_1'' > 0 \ , \tag{49}$$

where it is implied that in the lit side $\psi_1'' = \psi_2''$ and in the shadow side $\psi_2 = \overline{\psi_1}$. These conditions give the correct field behavior with $\xi < 0$ in the lit side, $\xi = 0$ at the caustic singularity, and $\xi > 0$ in the shadow side.

C. Root selection and ray-ordering modifications for dissipative media

The formalism presented above is not readily applicable to media with $\epsilon'' \neq 0$, as criterion (48) cannot be used to distinguish the lit and shadow regions. This is because, in general, we have $\psi_1' > \psi_2'$ in the caustic shadow. Two complex branch selections must be done in order to apply the EI in dissipative media: determination of the ray amplitudes (A_1, A_2) and of the Airy parameter ξ. The former requires one to determine which ray was reflected on the caustic, while the latter requires one to determine whether the current observation point sits on the lit or shadow side of the caustic.

1. Ray-ordering for amplitude branch selection

In the case of a fold caustic, reflected rays possess longer travel times than nonreflected rays. This is notably illustrated in Sec. IV. The ray-ordering criterion is then:

$$|\tau_1| < |\tau_2| \ , \tag{50}$$

$$||\tau_1| - |\tau_2|| > \delta_{\text{prec}} \ , \tag{51}$$

where we have introduced the small numerical parameter δ_{prec}, whose magnitude depends on the precision of the inverse Newton step. While Eq. (51) is well defined in most cases, numerical precision issues in nondissipative medium and being very close to the caustic can cause rays that should be identical to have slightly different parameters[37]. Given the convergence accuracy of the IRT Newton step of 1Å in ray position, we have found that $\delta_{\text{prec}} \simeq 1 \times 10^{-3}$ μm is required (where τ is usually of the order of 100 to 1000 μm). Application of the EI when criterion (51) is not satisfied is detailed in Sec. III E. Selection rule (50) implies that ray 2 was reflected on the caustic, so that the correct root for amplitude A_2 is the one that provides a $-\pi/2$ phase shift compared to A_1.

2. Root selection for the Airy parameter

The root selection for the Airy parameter ξ requires one to determine if a given observation point sits in the shadow or lit side. In the IRT framework, this criterion must be uniquely derived from the phase and amplitude information of the two rays at the observation point and must be valid in the case of $\epsilon'' = 0$ (e.g., be asymptotically equivalent to Eq. (48)). The difficulty arises from the fact that for $\epsilon'' \neq 0$, the caustic singularity $\xi = 0$ is no longer located in physical space (as shown in Sec. IV B 2). In that case, we deal with so-called *complex caustics*[32]. While the divergence point is not in physical space, divergent-like behavior of the rays is still observed in the caustic zone (i.e., for $|\psi_1 - \psi_2| \leq \lambda_0/2$), which usually intersects real space.

The following criterion for characterizing the shadow region when $\epsilon'' > 0$ was derived from tracing phases of CGO rays in dispersive linear permittivity profiles, as shown in Sec. (IV B 2):

$$\begin{aligned} \text{shadow region}: \ & \psi_1' - \psi_2' + \psi_1'' - \psi_2'' > 0 \ , \\ & \text{and} \quad \psi_1' - \psi_2' > 0 \ , \end{aligned} \tag{52}$$

where rays 1 and 2 were ordered according to relation (50).

From the knowledge of the observation point position with respect to the caustic shadow, the following root selection criterion is applied to ξ:

$$\begin{aligned} \text{lit region}: \ & \xi' < 0, \ \xi'' < 0 \ , \\ \text{shadow region}: \ & \xi' > 0, \ \xi'' < 0 \ , \end{aligned} \tag{53}$$

which is equivalent to selecting branches of ξ that do not produce exponential growth of the field in the caustic shadow.

D. Etalon Integral for GO rays in dissipative media

Application of the EI in dissipative media with GO rays also warrants a modification of the method formalism. This is because near caustics and in dissipative media, the difference in perturbative terms $\psi^{(1)}$ of the GO rays becomes large compared to the difference in unperturbed terms $\psi^{(0)}$. The associated loss of accuracy prevents the EI from converging for low values of $|\xi|$. A satisfying approximate solution, converging to $u = 0$ at $\xi = 0$, is obtained by using $\psi^{(0)}$ only in the EI to compute ξ and χ. Dissipation is then obtained by factoring $\exp -k_0\psi^{(1)}$ into the amplitude terms A_{0i}. This is illustrated alongside examples of wave propagation in permittivity profiles in Sec. IV B 4.

E. Indistinguishable rays for the Etalon Integral

We consider that rays reaching an observation point are numerically indistinguishable for the EI method when condition (51) is not satisfied. In general, this case is specific to CGO rays propagating close to caustics when $\epsilon'' = 0$. In these occurrences, ray 1 is defined such that $\psi_1'' < 0$. The ray phase and amplitude of the second ray are overwritten as $\psi_2 = \overline{\psi_1}$ and $A_2 = -\imath\overline{A_1}$, respectively, and we set $\xi = ((3/2)k_0\psi_1'')^{2/3} \in \mathbb{R}$ ($\xi > 0$). The field is then computed normally using the EI (Eq. (45)).

F. Unphysical rays in dissipative media

In the caustic shadow, two complex rays reach every observation point. When $\epsilon'' = 0$, the phases of the rays

are complex conjugate. Consequently, the two rays describe an exponentially damped and an exponentially increasing solution. While only the exponentially damped solution is physical ($\psi'' > 0$), both rays are mathematically justified and must be kept when applying the EI.

When computing the ray field without using the EI, the unphysical CGO ray in the caustic shadow must be discarded. This produces the correct field past the zone of CGO inapplicability (Eq. (43)). In strongly dissipative media however, both complex rays may be such that $\psi'' > 0$ in the caustic shadow. In that case, it is not possible to distinguish the physical from the unphysical ray, and only the application of the EI allows one to compute the field correctly. This is illustrated in Sec. IV B 2.

IV. ACADEMIC CASES

We now illustrate how complex rays propagate in various simple configurations and verify the accuracy of the EI fields against reference solutions. Apart from analytical solutions, numerical results for GO and CGO propagation are obtained with *IFRIIT*, for which a simplified workflow overview is given in App. 1. All numerical results are given for 351 nm laser light.

A. Assessment of GO and CGO differences due to the imaginary component of the dielectric permittivity

Comparisons of GO and CGO are conducted in 1-D in order to identify situations when the treatment of ϵ'' in GO is incorrect. For simplicity, homogeneous media separated from vacuum by discrete interfaces are considered. This allows one to use analytical solutions for CGO by simply applying the discrete jump conditions derived in Sec. II C 8.

1. Analytical solution for the electric fields

Consider a half space $x' > 0$ populated by a constant density medium of dielectric permittivity ϵ, otherwise surrounded by vacuum for $x' \leq 0$. A plane-wave is incident along the x' axis, with initial momentum $p_0 = 1$, amplitude $A_0^0 = 1$, and position $r_0 = 0$ in vacuum. In these conditions, the initial ray divergence is $D_0 = 1$. The ray position and momentum after the discrete interface are denoted $r_1 = r_0$ and p_1, respectively. The solution for τ at real space position x' is $\tau = (x' - r_1)/p_1$, which can be simplified to:

$$\begin{aligned}\tau_{\mathrm{GO}} &= x'/\sqrt{1 - n_\mathrm{e}/n_\mathrm{c}} = x' \,\mathrm{Re}(\epsilon)^{-1/2} \ , \\ \tau_{\mathrm{CGO}} &= x'/\sqrt{1 - n_\mathrm{e}/n_\mathrm{c}/(1 + \imath\nu_{\mathrm{IB}}/\omega_0)} = x'\epsilon^{-1/2} \ . \end{aligned} \quad (54)$$

The corresponding ray fields are:

$$|u|_{\mathrm{GO}}(x') = |\,\mathrm{Re}(\epsilon)|^{-1/4} \exp\left(-k_0 x' \frac{\mathrm{Im}(\epsilon)}{2\,\mathrm{Re}(\epsilon)^{1/2}}\right) \ , \quad (55)$$

$$|u|_{\mathrm{CGO}}(x') = |\epsilon^{-1/4}| \exp\left(-k_0 x' \,\mathrm{Im}(\epsilon^{1/2})\right) \ , \quad (56)$$

where we have used $D_0/D(\tau) = 1/p_1$ in this simple configuration. These equations illustrate how GO and CGO may predict different absorption in a constant-density plasma, where the ray divergence and absorption length are modified by $\mathrm{Im}(\epsilon)$. Before applying these formulas to various cases, we must discuss the form taken by ϵ in plasmas, and the usual assumptions that are made in laser propagation models.

2. On the form of the dielectric permittivity function

The plasma dielectric permittivity in presence of laser absorption by Inverse Bremsstrahlung reads[33]:

$$\epsilon = 1 - \frac{n_\mathrm{e}}{n_\mathrm{c}} \left(1 + \imath \frac{\nu_{\mathrm{IB}}}{\omega_0}\right)^{-1} \ , \quad (57)$$

where ν_{IB} is the Inverse Bremsstrahlung collision frequency.

In the standard GO framework, where it is assumed that $\epsilon'' \ll \epsilon'$, the assumption $\nu_{\mathrm{IB}} \ll \omega_0$ is commonly made. The corresponding permittivity reads:

$$\epsilon_{\nu_{\mathrm{IB}} \ll \omega_0} = 1 - \frac{n_\mathrm{e}}{n_\mathrm{c}} + \imath \frac{n_\mathrm{e}}{n_\mathrm{c}} \frac{\nu_{\mathrm{IB}}}{\omega_0} \ . \quad (58)$$

While it is natural to make use of Eq. (57) for CGO, many GO-based models rely on Eq. (58). The ratio $\mathrm{Re}(\epsilon)/\,\mathrm{Im}(\epsilon)$, which must be $\gg 1$ for GO validity with respect to CGO, is shown in Fig. 3. In these graphs, ν_{IB} is computed as a function of electron temperature T_e, for a CH plasma with effective ionization $< Z^2 > / < Z >$=3.1 and ion temperature $T_i = T_e$. Using the simplified formulation for the permittivity leads to a large domain where $\mathrm{Re}(\epsilon) \gg \mathrm{Im}(\epsilon)$ is not satisfied. In that region, GO will deviate significantly from CGO because of the formulation of the dielectric permittivity. A more relevant comparison is to make use of the non-simplified permittivity in the GO approach. In that case, it can be expected that GO will fail compared to CGO in the density/temperature region highlighted in Fig. 3 (b), i.e. intermediate temperature plasma at high density. At high temperatures, above 1 keV, the domain of GO inapplicability remains confined to the critical density region, which incidentally coincides with the caustic region for rays at normal incidence. This case is discussed extensively in Sec. IV B.

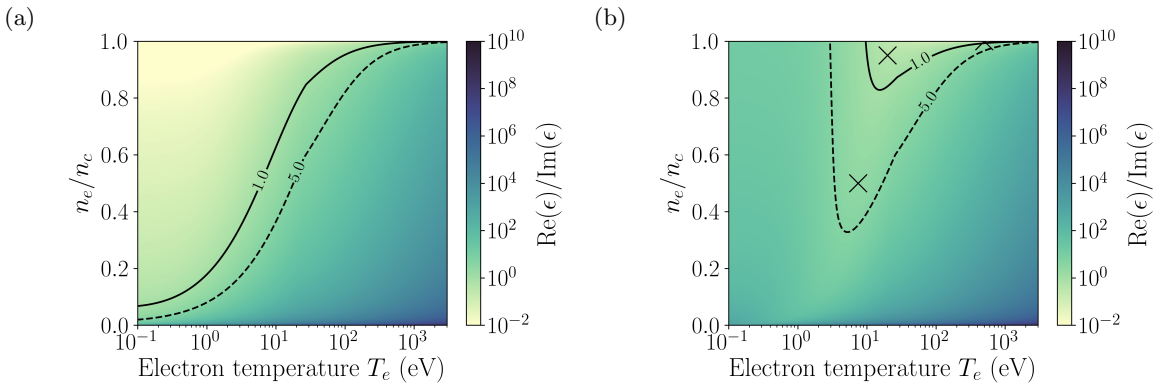

FIG. 3. Ratio of the real to imaginary part of the dielectric permittivity, (a) with and (b) without the assumption $\nu_{\mathrm{IB}} \ll \omega_0$. The Inverse Bremsstrahlung collision coefficient ν_{IB} is computed from the electron-ion collision coefficient[33] and using typical formulations for the Coulomb logarithm as implemented in radiative hydrodynamic codes. The permittivities are expressed as a function of electron temperature T_e and electron number density normalized to the critical density n_e/n_c. At low temperatures, loss of collisionality due to Fermi degeneracy is approximated by substituting T_e with $\sqrt{T_e^2 + T_f^2}$, where the Fermi temperature $T_f = (3\pi^2 n_e)^{2/3}\hbar^2/(2m_e k_b)$. The solid and dashed lines show the $\mathrm{Re}(\epsilon) = \mathrm{Im}(\epsilon)$ and $\mathrm{Re}(\epsilon) = 5\,\mathrm{Im}(\epsilon)$ contours, respectively. Crosses in (b) correspond to the absorption cases presented in Sec. IV A 3: $T_e = [7.5, 20, 500]$ eV and $n_e/n_c = [0.5, 0.95, 0.9998]$. The corresponding Inverse Bremsstrahlung coefficient is $n_e\nu_{\mathrm{IB}}/(n_c\omega_0) = [0.42, 0.35, 0.008]$.

3. Absorbing medium

The difference in absorption between GO and CGO is illustrated at three points highlighted in Fig. 3 (b): (a) cold plasma of intermediate density $T_e = 7.5$ eV, $n_e/n_c = 0.5$, corresponding to $n_e\nu_{\mathrm{IB}}/(n_c\omega_0) = 0.42$, (b) cold plasma at high density $T_e = 20$ eV, $n_e/n_c = 0.95$, corresponding to $n_e\nu_{\mathrm{IB}}/(n_c\omega_0) = 0.35$ and (c) warm plasma at close-to-critical density $T_e = 500$ eV, $n_e/n_c = 0.9998$, corresponding to $n_e\nu_{\mathrm{IB}}/(n_c\omega_0) = 0.008$. We consider the cases of GO using the non-approximated and approximated permittivities (Eqs. (57) and (58), respectively). The CGO case makes use of the non-approximated permittivity. Corresponding results are given in Fig. 4.

In all cases, the fields from GO with approximated permittivity greatly overestimate the laser absorption, which is due to $\mathrm{Im}(\epsilon)_{\nu_{\mathrm{IB}} \ll \omega_0} > \mathrm{Im}(\epsilon)$. This is observed in a wide range of plasma parameters and must be carefully accounted for in laser models. In the cold plasma and intermediate density case (Fig. 4 (a)), corresponding to $\mathrm{Re}(\epsilon) = 2.7\,\mathrm{Im}(\epsilon)$, the GO and CGO fields computed using ϵ are in agreement. A discrepancy appears in the higher density cases (cold and warm plasmas, Fig. 4 (b,c)), where GO overestimates absorption. This difference is related to the ray momentum that shifts into complex space in the CGO case which shortens the effective absorption length. In general, GO may remain invalid at high temperatures for densities sufficiently close to the critical density, but these regions are narrow since rays quickly refract out of high densities.

To summarize these results; GO is valid for cold plasma as long as the non-approximated formulation for the permittivity is used (Eq. (57)). GO becomes invalid in an intermediate temperature regime, where it over-predicts absorption. This is consistent with usual trends of hydrodynamic codes overestimating absorption at early times in ICF implosions. Finally, at high temperatures, GO is only invalid in a highly narrow region around the critical density, which is a good approximation in most cases. These conclusions are drawn only for plane-waves, so that the initial phase is the same in both GO and CGO. Additionally, we show in Sec. IV B 4 that GO suffers from limitations at caustics in dissipative media, which are not related to the validity condition $\epsilon'' \ll \epsilon'$ but to the one on the phases, $\psi^{(1)} \ll \psi^{(0)}$.

B. Complex ray propagation through caustics

We have highlighted how CGO gives more accurate solutions for fields in cases where $\epsilon'' \sim \epsilon'$. We now illustrate how CGO can be used to compute laser fields close to and behind caustics. CGO solutions are obtained by applying the 3-D finite-element complex ray-tracing algorithm described in Sec. II in a simple plane-wave 1-D configuration. The accuracy of the model and of the EI technique for caustic fields is assessed by comparisons to the nonparaxial electromagnetic wave propagation code *LPSE*[34].

1. Nonabsorbing density ramp

Consider a plane-wave propagating from the initial position $r_0 = 0$ with initial momentum $p_0 = 1$ and vacuum intensity $I_0 = 10^{14}$ W/cm^2 into a constant density gradient in the absence of dissipation, such that $\epsilon = 1 - x/L$ with $L = 95.9$ μm. For a GO ray, we have $x = x' \in \mathbb{R}$.

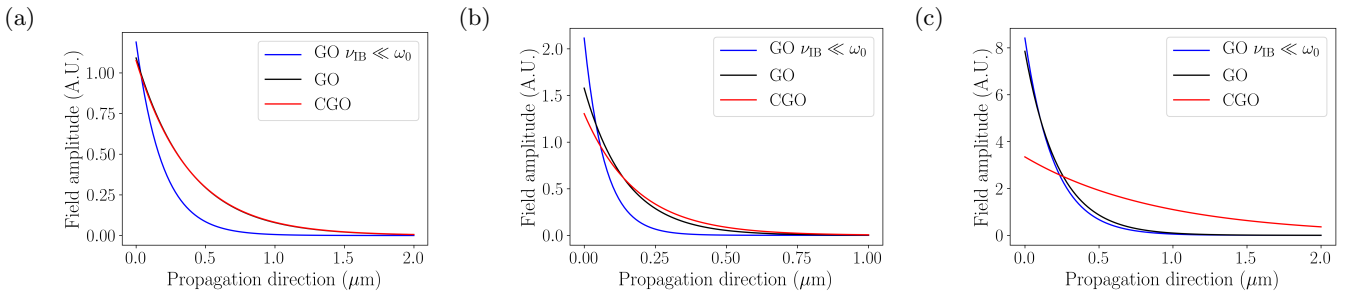

FIG. 4. Ray absorption in a constant dielectric permittivity medium, for (a) cold plasma of intermediate density $T_e = 7.5$ eV, $n_e/n_c = 0.5$, corresponding to $n_e\nu_{IB}/(n_c\omega_0) = 0.42$, (b) cold plasma at high density $T_e = 20$ eV, $n_e/n_c = 0.95$, corresponding to $n_e\nu_{IB}/(n_c\omega_0) = 0.35$ and (c) warm plasma at close-to-critical density $T_e = 500$ eV, $n_e/n_c = 0.9998$, corresponding to $n_e\nu_{IB}/(n_c\omega_0) = 0.008$. Fields from GO and CGO using the non-approximated permittivity (Eq. (57)) are shown as black and red lines, respectively. The corresponding GO result using the approximated permittivity (Eq. (58)) is shown as blue lines. The amplitude jump observed at coordinate $x = 0$ is due to the vacuum/plasma interface. GO and CGO results are on top of each other in (a).

This is also the case when integrating the ray equations in CGO with $\alpha = 0$. In the general CGO case however, the dielectric permittivity is defined with $x \in \mathbb{C}$ in order to satisfy the Cauchy Riemman conditions (see Sec. II B 4). In both cases, the permittivity gradient is real valued and $\boldsymbol{\mathcal{G}}_\epsilon = -1/L$. For simplicity, the real-space spatial coordinate x' is taken along $\mathbf{p}_0$, e.g., the wave is at normal incidence.

The analytical solution is obtained by solving Eq. (28) for $\mathbf{r}'(\tau).\mathbf{p}_0 = x'$ with $\boldsymbol{\mathcal{G}}''_\epsilon = 0$:

$$\tau = 2L(1 \pm \sqrt{1 - x'/L}) \ . \tag{59}$$

Equation (59) possesses at most two solutions, corresponding to the overlap of incoming and outgoing waves. In both GO and CGO, only one solution exists at $x' = L$. This degeneracy in the number of solutions is a caustic. In the framework of GO, the condition $x' \leq L$ must be always met. This defines a region of space where no GO solution exists. This is the caustic shadow, characterized here with $x' > L$.

It is straightforward to understand how the limitations of ray propagation are lifted when considering CGO trajectories. Since the ray parameter can be complex valued, equation (59) always has one or two solutions ($x' = L$ still represents a caustic). In the lit area, $\sqrt{1 - x'/L} \in \mathbb{R}$ so that $\tau \in \mathbb{R}$ and the ray propagates with $\alpha = 0$ in real space. In the shadow area, $\tau \in \mathbb{C}$ so that the ray propagates from the initial real position into complex space and back to real space. This is illustrated in Fig. 5 for a case with $L = 95.9$ μm: rays effectively bypass the divergence point located in real space by undergoing an excursion into complex space.

The electric field is obtained by adding the individual ray field and compared to *LPSE*. The CGO ray field in the linear permittivity profile is shown in Fig. 6. Without applying the EI, the ray field diverges in a region around the caustic where the phase difference between the rays is less than $\sim \lambda_0/3$. Applying the EI method in the caustic region, the caustic field is recovered. The resulting fields are in agreement with the reference solution from *LPSE* and the analytical result, in the entire space, including in the caustic shadow. Finally, we note that by summing the interfering fields directly, the ray solution is able to capture the corresponding amplitude oscillation.

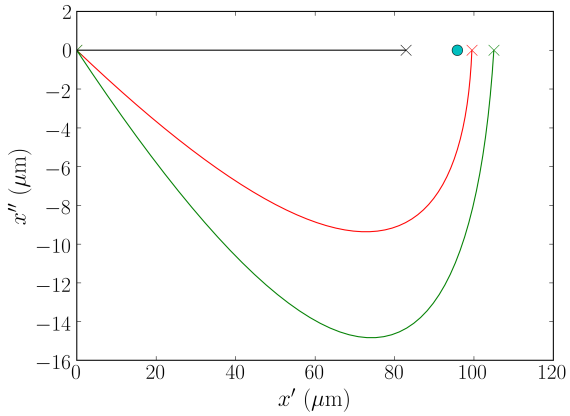

FIG. 5. Ray trajectories in complex space for real-space end points x' in the lit region (black) and in the shadow region (red and green). The starting and end points of complex rays are indicated by colored x's. The caustic location is indicated with a cyan circle.

2. Complex caustics in dissipative media

We now consider the case of dissipative media ($\epsilon'' > 0$), such that CGO rays in the lit area also shift in complex space. The dielectric permittivity is set to $\epsilon = 1 - x/L + \imath(x/L)^2\nu^*_{IB}/\omega_0$ with $L = 95.9$ μm and ν^*_{IB} is the Inverse Bremsstrahlung (IB) frequency at the critical density ($\nu_{IB} = n_e/n_c\nu^*_{IB}$). Here, the profile for ϵ'' is

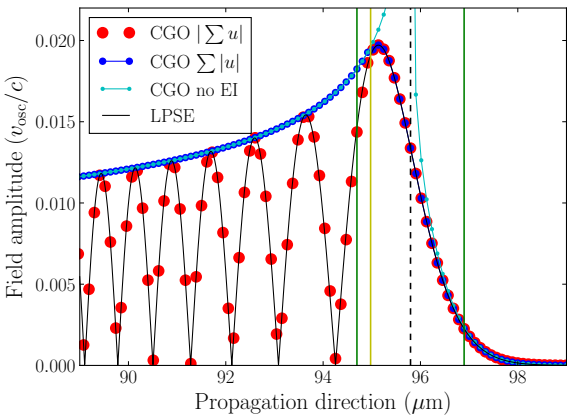

FIG. 6. Field amplitude in a non-absorbing linear permittivity profile near the caustic location. The numerical solution from *LPSE* is shown as a black curve. The spatial region of ray optics inapplicability (Eq. (43)) exists between the two vertical green lines. The caustic divergence location $\xi = 0$ is shown as a vertical dashed black line. Non-interfering fields obtained with CGO with and without application of the EI method are shown as blue and cyan dotted lines, respectively. Interfering fields are shown as red dots. The EI is applied to the right of the vertical yellow line, corresponding to the criterion $|\psi_1 - \psi_2| \geq \lambda_0/3$.

parabolic, which departs from the subgrid assumptions of *IFRIIT* (see Secs. II and III). Two absorption cases are considered: weakly dissipative media with $\nu^*_{\rm IB} = 2/\text{ps}$ ($\nu^*_{\rm IB}/\omega_0 = 3.72 \times 10^{-4}$) and moderately dissipative media with $\nu^*_{\rm IB} = 20/\text{ps}$ ($\nu^*_{\rm IB}/\omega_0 = 3.72 \times 10^{-3}$), covering a range relevant to ICF conditions. Note that in these conditions, the region of GO inapplicability due to $\epsilon'' \geq \epsilon'$, discussed in Sec. IV A 3, is only located in a narrow region at the critical density.

The introduction of dissipation affects the phase and complex parameters of rays reaching the real-space observation points. Notably, absorption decreases the real part of the ray path-length τ' mostly in the caustic region and caustic shadow, while the imaginary part of the ray path-length increases in the lit area and caustic region. These tendencies, shown in Figs. 7(a) and 7(b), justify the ray-ordering criterion proposed in Eq. (50). In addition, the physical points at which $\psi'_1 = \psi'_2$ and $\psi''_1 = \psi''_2$ no longer coincide and grow farther apart with increasing absorption, as shown in Fig. 7(c). This corresponds to the embedding of the caustic in complex space: $\xi = 0$, corresponding to $\psi_1 = \psi_2$, is located in complex space. Said differently, there is no observation point in physical space where the ray mapping degenerates from two rays ($\psi_1 \neq \psi_2$) to one ray ($\psi_1 = \psi_2$). For modest dissipation, however, the caustic region still intersects real space. This is shown in Fig. 7(c) where the complex trajectory of the phase difference intersects with the inapplicability region of the ray optics framework for $\nu^*_{\rm IB} = 2/\text{ps}$ and $\nu^*_{\rm IB} = 20/\text{ps}$. Conversely, for a sufficiently dissipative medium, this trajectory no longer intersects the inapplicability region in real space, e.g., the caustic region is completely embedded in complex space. This is illustrated for $\nu^*_{\rm IB} = 70/\text{ps}$ in Fig. 7(c). In that case, there is neither a caustic nor a caustic region for the CGO rays, and the fields are well defined everywhere, as shown in Fig. 7(d) for the CGO field without application of the EI. Careful examination of the phase differences as a function of space compared to the three branches for ξ was used to determine the exponentially damped solutions and the subsequent selection criterion given in Eq. (51).

We now compare the ray fields with *LPSE*. We show in Figs. 8(a) and 8(b) the GO and CGO results with and without the EI method, for $\nu^*_{\rm IB} = 2/\text{ps}$ and $\nu^*_{\rm IB} = 20/\text{ps}$. The caustic shift in complex space implies that the complex ray solution no longer diverges at the caustic in the presence of absorption (see notably Fig. 8(b) at the lit/shadow boundary), although it reaches an incorrect value. Furthermore, the unphysical ray selection rule can no longer be applied (see Sec. III F) and the CGO rays are an exponentially growing solution behind the caustic. The incorrect ray field in the caustic region and the unphysical solution growth are both successfully corrected by the modified EI using the ray parameters themselves.

3. Caustic fields in nonlinear density gradients

We now consider a Gaussian profile of the form $\epsilon = 1 - 1.2\exp\{-[(x - x_{\rm max})/L]^2\} + i1.2\exp\{-2[(x - x_{\rm max})/L]^2\}\nu^*_{\rm IB}/\omega_0$, with $L = 42.3$ μm and $x_{\rm max} = 115$ μm. In this case, the large-scale ϵ' profile is also nonlinear and departs from the sub-grid assumptions. This is a stringent test of the entire model implementation, including the EI formulation.

Results for CGO are reported in Fig. 8(c) for $\nu^*_{\rm IB}/\omega_0 = 3.72 \times 10^{-4}$, alongside the *LPSE* simulation. Excellent agreement is found between our implementation of CGO and the reference solution. These test cases show that CGO used in conjunction with an EI method adapted to dissipative media can be used to reproduce caustic fields in media with nonlinear ϵ' and ϵ''.

4. Modified Etalon Integral method for GO rays in dissipative media

In Sec. IV A 3, we have highlighted how the validity domain of GO in constant density media is related to the magnitude of ϵ'' and its discrete jump across interfaces. Given the derivation of GO in weakly dissipative media presented in Sec. II C 2, there is the additional assumption that $\psi' \gg \psi''$. While we have shown that for usual plasma parameters, GO is invalid only in a narrow region around the critical density, the picture is different in inhomogeneous media. Notably, in the caustic region, the EI relies on a parameter ξ that depends on the phase

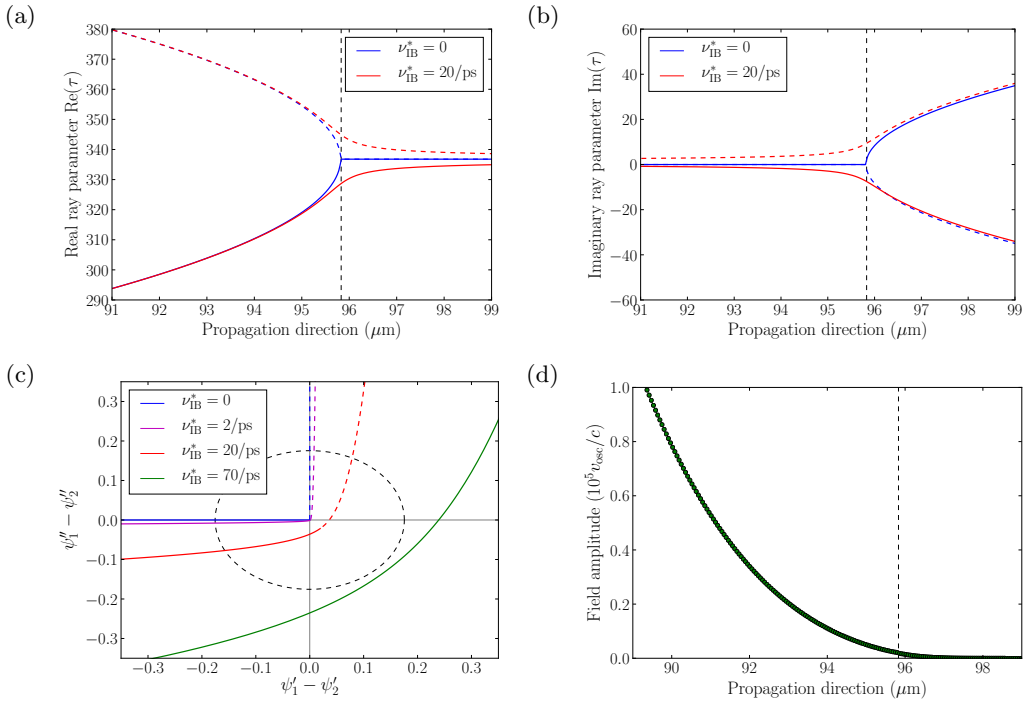

FIG. 7. Real part (a) and imaginary part (b) of the propagation parameter τ for rays reaching various real-space observation points in the caustic region. Parameters from incoming rays are shown as solid lines and from reflected rays as dashed lines. Calculations with $\nu^*_{\rm IB} = 0$ and $\nu^*_{\rm IB} = 20$/ps are shown in blue and red, respectively. The caustic location in the nondissipative case is shown as a vertical dashed black line. (c) Complex path of the phase difference $\psi_1 - \psi_2$ of rays reaching various real-space observation points in the linear layer. The caustic divergence point is located at $(0, 0)$, indicated by the intersection of two solid gray lines. The region of GO/CGO inapplicability is located inside the dashed black circle. Calculations with $\nu^*_{\rm IB} = 0$, $\nu^*_{\rm IB} = 2$/ps, $\nu^*_{\rm IB} = 20$/ps, and $\nu^*_{\rm IB} = 70$/ps are shown in black, blue, red, and green, respectively. Solid lines indicate the lit region and dashed lined the shadow region. (d) Fields obtained with CGO IRT with $\nu^*_{\rm IB} = 70$/ps. The caustic location in the nondissipative case is shown as a vertical dashed black line. No application of the EI is made in that case.

difference between the rays. Applications of the EI for GO shows that the reconstructed field diverges near the caustic in a region much larger than one defined by the simple assumption $\epsilon'' \ll \epsilon'$, as shown in Fig. 9. This is due to the loss of accuracy in GO for computing ξ in dissipative media and near the caustic, where we have $\psi'_2 - \psi'_1 \leq \psi''_2 - \psi''_1$. In other words, since GO is not able to model complex caustics, the fields obtained attempting to model a real caustic in dissipative media are discrepant with the CGO fields.

While the correct approach would be to use complex rays in the caustic region for dissipative media, it is convenient to use a modification of the EI for GO that avoids field divergence at the caustic point. Simply, the EI is computed as if the medium were non-dissipative, e.g., by using $\mathrm{Re}(\psi)$ to compute ξ and χ. The absorption term is then added in the amplitude factors, e.g., by substituting A_{0i} with $A_{0i} \exp\left[-k0\,\mathrm{Im}(\psi_i)\right]$. Resulting fields from the modified EI are shown in Fig. 9. The modified EI successfully compensates for the shortcoming of GO near the complex caustic.

The study of ray fields in inhomogeneous dissipative media presented here exhibits the advantages of CGO over GO for the caustic field. For plane-waves, and in typical ICF or HED plasmas, this advantage is mainly the computation of the fields in the shadow region and at the caustic boundary. Accurate computation of the caustic field is useful for AMR algorithms that may otherwise treat the lit/shadow boundary in GO as a steep gradient that must always be refined. Such algorithms, their synergy with the IRT framework, and their usefulness in CBET computations will be detailed in a following paper.

C. Gaussian beam diffraction

In previous sections, we have highlighted the capability of CGO to accurately model fields in situations where $\epsilon' \sim \epsilon''$ and $\nabla\epsilon' \sim \nabla\epsilon''$ and behind real and complex caustics. We now illustrate the usefulness of CGO in the case of beams with complex initial conditions. This is notably the case of Gaussian beams and beams smoothed by phase plates, which possess non-plane complex valued initial phase fronts.

A 2-D Gaussian wavefield in its focal plane can be written in complex form as $u_G(\zeta_1, 0) = \exp[-\zeta_1^2/(2w_0^2)]$. Recalling that the ray field is expressed as $u = A_0 \exp[\imath k_0 \psi]$,

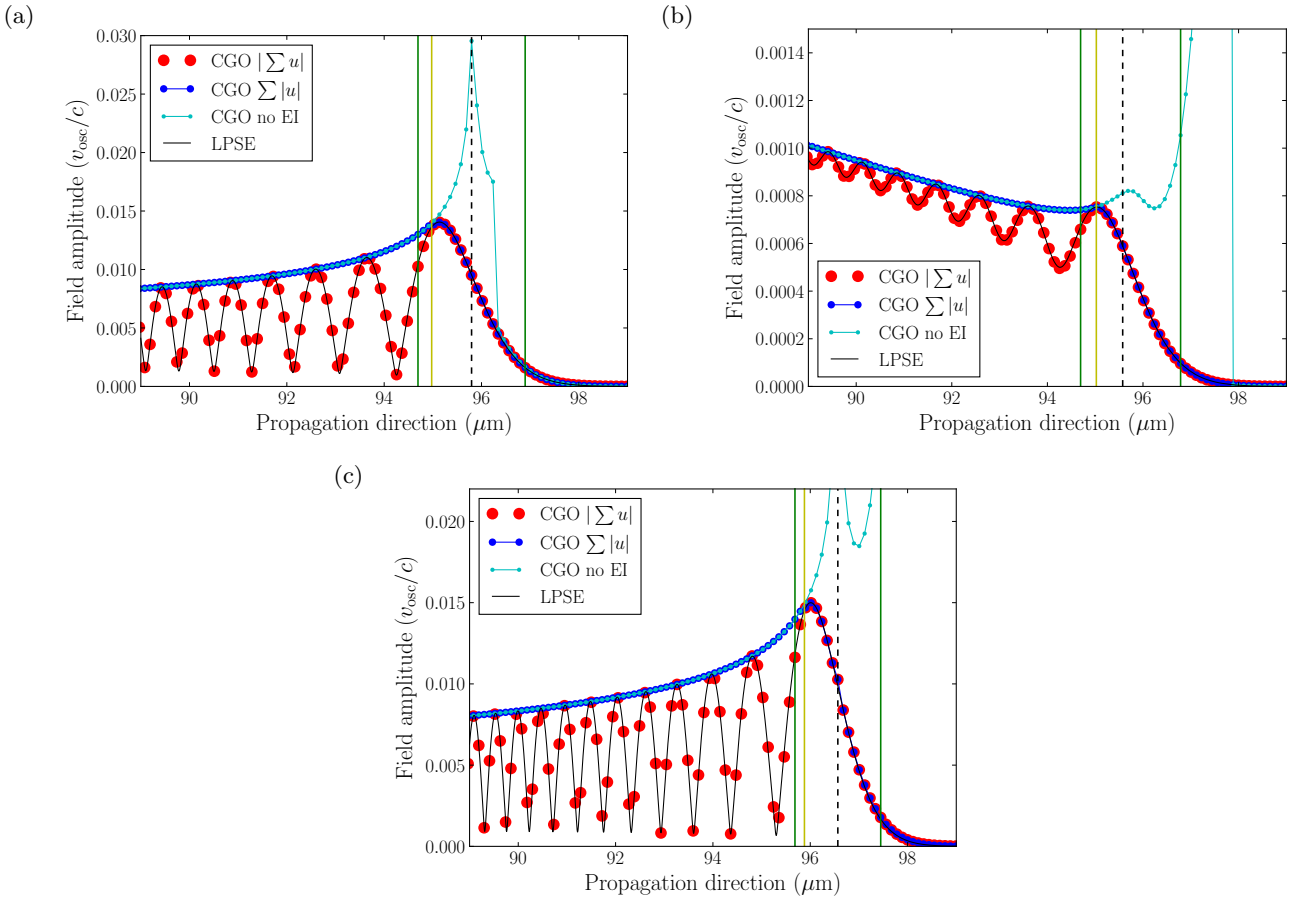

FIG. 8. Field amplitude in a [(a),(c)] weakly and (b) moderately absorbing medium near the caustic location, for a linear density profile [(a),(b)] and an exponential density profile (c). Curves are labeled as in Fig. 6.

it is readily seen that the GO initial conditions read $A^0_{0,\mathrm{go}} = \exp[-\zeta_1^2/(2w_0^2)]$ and $\psi^0_{\mathrm{go}} = 0$. Conversely, the CGO initial conditions may be written as $A^0_{0,\mathrm{cgo}} = 1$ and $\psi^0_{\mathrm{cgo}} = \imath\zeta_1^2/(2k_0w_0^2)$. As such, the rays in GO are initially parallel across the beam. In vacuum, propagation of these rays then yields a cylinder-like field with a Gaussian profile. In the CGO case, the initial momentum transverse to the beam direction has a non zero imaginary component derived from $p_x^0 = \partial\psi^{(0)}/\partial\zeta_1$. Propagation of complex rays following these initial conditions produces a field pattern that exactly follows that of a Gaussian beam undergoing diffraction, as shown in Fig. 10(a). As the beam propagates, the rays accumulate a complex phase such that the beam diffracts in the near field and then transitions to a spherical wave as it propagates farther, as can be seen in Fig. 10(b).

The capability of CGO to model diffraction of a Gaussian beam in vacuum was first shown in Refs. 32 and 35 and numerically applied to homogeneous media in Ref. 28. Potential applications in ICF are related to diffraction modeling of beams with non-plane initial phase fronts, such as beams smoothed by phase plates, although this remains to be demonstrated. This contrasts with the artificial diffraction-like approaches used in GO-based ray-tracing in ICF hydrodynamic codes, where the initial k-vector of the plane-wave is spread at the lens to artificially mimic a beam diffraction pattern.

D. 2-D field computation in a Gaussian density profile

We now present an application of *IFRIIT* to plane-wave field computation in an ICF-like density profile. The plasma density is set to:

$$\frac{n_\mathrm{e}}{n_\mathrm{c}} = 4\exp\left[-\frac{(x-x_{\max})^2+(z-z_{\max})^2}{L^2}\right], \qquad (60)$$

with $L = 83.6$ μm and $x_{\max} = z_{\max} = 25$ μm. The IB frequency at the critical density is set to $\nu^*_{\mathrm{IB}}/\omega_0 = 7.45\times10^{-3}$. The density profile is Gaussian in the (x,z) plane and invariant along the y direction, to facilitate comparisons with *LPSE*. The beam is incident along the x axis and centered around $z = 25$ μm, with a radial profile of super-Gaussian order 4 and radius at 1/e of 100.9 μm. The vacuum intensity is 3×10^{15} W/cm^2 and the wavelength is 351 nm.

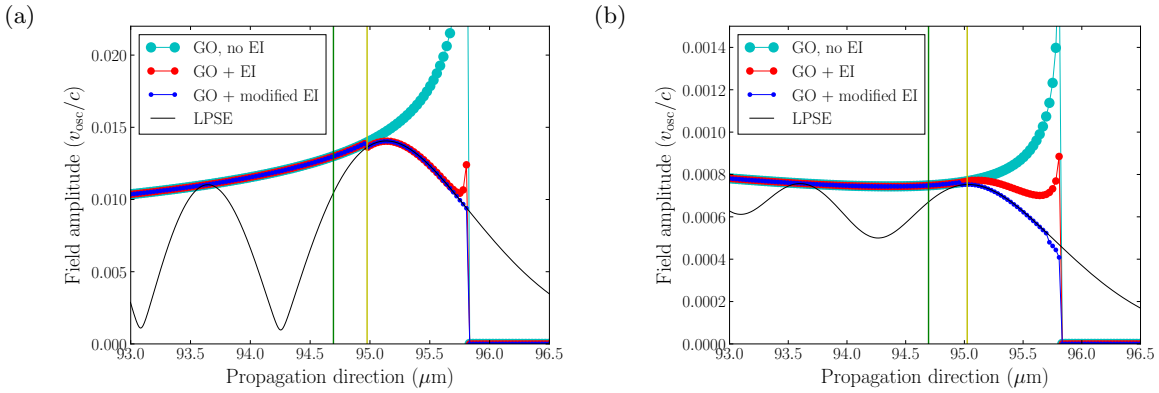

FIG. 9. Field amplitude in (a) a weakly and (b) a moderately absorbing medium near the caustic location, for a linear density profile. Numerical solutions from *LPSE* are shown as black curves. The spatial region of ray optics inapplicability (Eq. (43)) is located right of the vertical green line. Non-interfering fields obtained with GO and without the EI method are shown in cyan. Corresponding results using the baseline and modified EI method are shown in red and blue, respectively. The EI is applied right of the vertical yellow line, corresponding to criterion $|\psi_1 - \psi_2| \geq \lambda_0/3$.

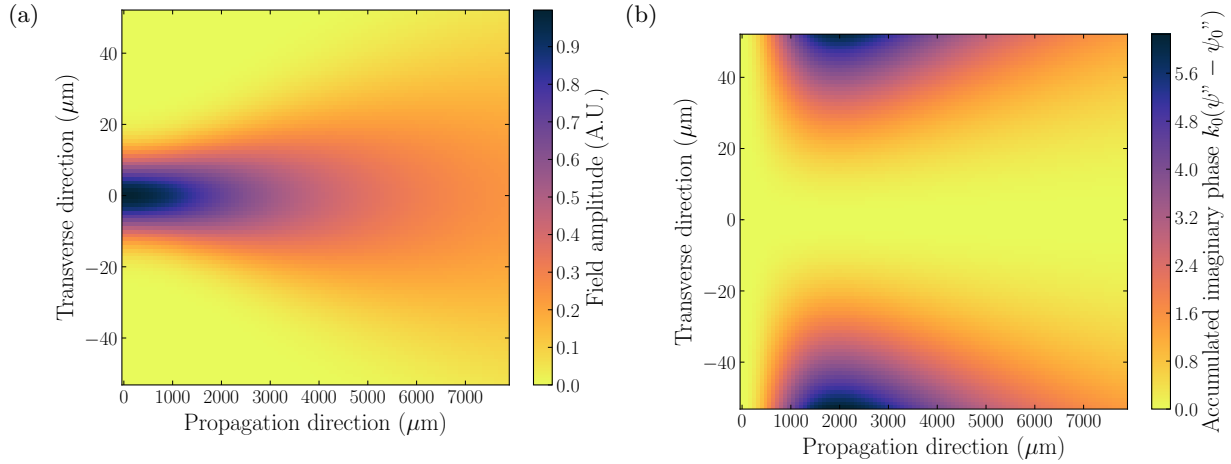

FIG. 10. Propagation of CGO rays with an initial condition of a Gaussian wavefield with initial radius $w_0 = 30\lambda_0$. Rays are propagated up to $\sim 8a_r$, where $a_r = 992$ μm is the Rayleigh range. (a) Field amplitude in the simulation box. (b) Imaginary phase accumulated along the CGO ray propagation.

1. Fields in the coronal plasma

Fields are computed using the GO IRT model with modified EI. Given the results presented in Secs. IV A 3 and IV B 4, the only discrepancy to be expected compared to CGO lies in the shadow region of the caustic. The permittivity profile is discretized using a 3-D tetrahedral mesh with N_rxN_yxN_θ=401x3x801 vertices uniformly meshed on a cylinder of 205-μm radius and height. Fields in *IFRIIT* are computed at the tetrahedron vertices and shown alongside *LPSE* results in Fig. 11(a). Corresponding profiles along the $n_e/n_c \in [0.05, 0.25, 0.65]$ isocontours are given in Fig. 11(b). Excellent agreement is obtained in the entire coronal plasma. Notably, the region of high laser refraction features a dip in the electric field along the $n_e/n_c = 0.05$ contour that is particularly challenging to capture using rigid-scale estimators commonly implemented in hydrodynamic codes since ray statistics converge slowly in such regions. The IRT method successfully reconstructs this part of the field without additional cost. The caustic fields are also well reproduced, although they are largely under-resolved despite the high angular resolution employed here. In practice, one would rely on AMR to resolve the caustic scales.

2. Resolution scaling of the caustic solution

The GO IRT solution presented above was obtained using uniform mesh spacing in the radial and angular directions. In a practical inline calculation with *IFRIIT*, one would use a lower resolution in the coronal plasma and use AMR in regions of interest, e.g., regions of high

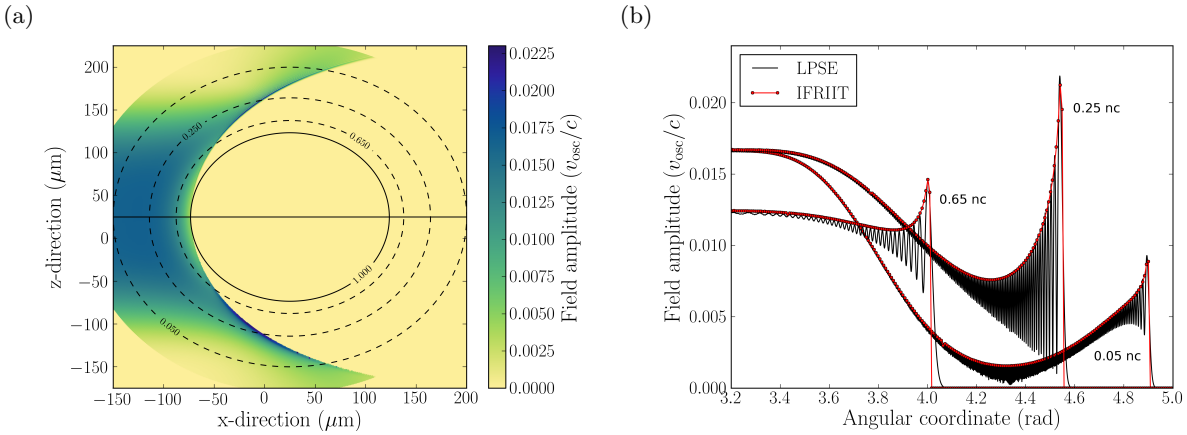

FIG. 11. (a) Fields computed from *LPSE* (top half) and the *IFRIIT* GO model (bottom half), separated by a horizontal line at $z = 25$. Fields from the IRT GO model are shown at the vertices of the tetrahedral mesh in the $y = 0$ plane. All fields are cut off below 0.001 n_c. Dashed black lines highlight the locations of the 5%, 25%, and 65% critical-density contours, respectively. The critical density position is shown as a solid black line. The thickness of the caustic in the IRT GO model appears larger than it is due to the plotting procedure (see profiles in (b)). (b) Field profiles along the 5%, 25%, and 65% critical-density contours as functions of the angular coordinate where π corresponds to the input beam direction. *LPSE* simulations are shown in black and GO IRT fields are shown as dotted red lines.

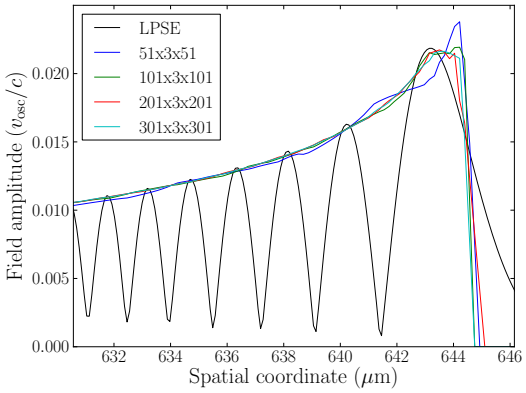

FIG. 12. Caustic fields along the 0.25 critical-density contour between *LPSE* (black line) and *IFRIIT* using real-valued rays (colored lines). Mesh resolutions correspond to those given in Table I.

N_rxN_yxN_θ	Δr (μm)	$\Delta\theta$ (°)
51x3x51	4	7
101x3x101	2	3.6
201x3x201	1	1.8
301x3x301	0.7	1.2

TABLE I. Mesh configuration employed for the scaling simulations. The number of vertices N_{rc}xN_yxN_θ is indicated in the r, y, and θ directions, respectively. The grid is uniformly spaced in $r = \sqrt{x^2 + z^2}$ and $\theta = \tan^{-1}(z/x)$, with corresponding resolutions Δr and $\Delta\theta$. Three grid points are employed in the y direction, with no gradients in that direction.

CBET gain gradients or high field gradients such as caustics (see App. 1 for more details). Employing a low resolution in the corona could lead to an accumulation of error in the ray phase that would degrade the adaptively refined caustic solution. Here, we present a grid resolution scaling of the coronal plasma discretization to illustrate how the caustic field is affected.

The caustic field is diagnosed by inserting observation points along the $n_e/n_c = 0.25$ density contour. These points are not tied to tetrahedrons and as such do not modify the subgrid dielectric permittivity profile: they are a synthetic diagnostic, for which the IRT method is well suited. The mesh resolutions considered here are detailed in Table I. Corresponding results are given in Fig. 12. The solution is seen to converge to satisfactory accuracy for resolutions of $\Delta r = 2$ μm and $\Delta\theta = 1.8°$. The value for Δr is to be compared with the inhomogeneity scale length of this case and will be relaxed correspondingly for longer scale-length plasmas. Note here that the converged position and shape of the caustic differ slightly from the solution from *LPSE*: the caustic location is shifted by ~ 0.4 μm, the peak amplitude is the same, and the caustic is more spread out in the *LPSE* case. While this accuracy is deemed sufficient, we mention that the discrepancy is due, in part, to the difficulty of converging the *LPSE* solution in regions where rays approach a caustic wih glancing angle of incidence. Higher-resolution runs suggest that the caustic location is converging toward the ray solution, albeit at a slow rate. For reference, the *LPSE* run took 32.7 hours on 360 cores. Runtimes for *IFRIIT* are discussed in Sec. IV D 3.

These results suggest that intermediate mesh resolutions may be used in the coronal plasma while still retaining sufficient accuracy in the caustic region. The caustic region itself may then be resolved using AMR at wavelength scales.

3. Performance scaling

We now discuss performance of the *IFRIIT* code in the 2-D Gaussian case. Several caveats must be underlined. First, the model implementation is currently not fully optimized since it is in a development state that facilitates experimentation and debugging. Second, the 2-D plasma configuration is computed on a 3-D mesh, implying that the tracing algorithms are largely under-optimized for a 2-D configuration, including all arc-length calculations and vector operations. Finally, there is an important distinction between initialization of the IRT procedure and timestepping. Namely, initialization requires CPU- and memory-intensive algorithms to find all rays converging to the mesh vertices. This computation cost is relaxed when considering timestep iterations, where the IRT initial guess can be taken from the previous timestep.

As was discussed throughout the paper, *IFRIIT* aims at being implemented as an inline module in radiative hydrodynamic codes, and significant simplifying assumptions have been made to that end. As such, it remains relevant to mention the order of magnitude of the performance with the current model implementation. Timing results from the resolution scaling study (Sec. IV D 2) are reported in Table II. The initialization time t_{init} includes the construction of the 3-D initial guess map (function $\mathbf{G} : (\zeta_1, \zeta_2, \tau)$ in Sec. II A 2), application of the 3-D minimum filter, Newton iteration on all guesses and determination of which points are in the caustic shadow, which is costly in GO since it involves the non-convergence of the IRT Newton step. The timestepping time t_{step} is estimated as the time it takes to conduct one Newton iteration on all the observation points in the lit side. The field computation time t_{fields} includes tracing of the rays to each observation point with integration of phase and amplitude, as well as application of the EI algorithms. All times reported here are total CPU time and therefore do not account for parallelization. The code was compiled using the GNU Compiler Collection (GCC) with simple O2 optimization.

The results are compatible with the performance requirements for an inline implementation in a radiative hydrodynamic code. Timestepping and field computation time are under a minute on a single CPU, even at high resolutions. Performance scaling when adding tetrahedrons in the third dimension (here along y) will require an Message Passing Interface implementation. It is estimated that the number of compute nodes typically used for 3-D hydrodynamic calculations will be compatible with the requirements of *IFRIIT*. The cost of using CGO over GO is in general 0-30% higher. However, achieving the same accuracy in highly non-linear permittivity profiles require a finer meshing for CGO due to the discrete jump conditions (see Sec. II C 8), which significantly increase the effective computation and memory cost. This is discussed in App. 2.

V. CONCLUSION

We have described an accurate method of modeling laser fields at hydrodynamic scales. The model combines an Inverse Ray-Tracing (IRT) method with a piecewise linear dielectric permittivity approximation within a 3-D tetrahedral mesh to compute fields at arbitrary observation points within the simulation domain. By choosing the observation points to be the tetrahedron's vertices of the mesh, the piecewise linear approximation can be extended to all laser-related quantities. This approach allows for convenient implementation of nonlinear laser-plasma interactions models.

Laser fields can be computed with the IRT by using either conventional Geometrical Optics (GO) or Complex Geometrical Optics (CGO). We have demonstrated how CGO extends the validity domain of GO in conditions where the imaginary part of the dielectric permittivity overcomes the real part. In typical ICF plasmas, this is notably the case at intermediate temperatures and at high temperatures close to the critical density, where GO overestimates absorption. Additionally, using GO with the usual approximated expressions for the permittivity produces large discrepancies between GO and CGO at low temperatures. This particular occurrence is corrected by using the non-approximated expression for the permittivity. These trends are consistent with usual observations made in ICF experiments where hydrodynamic codes tend to overestimate absorption at early times. Finally, we have illustrated how CGO exactly models the diffraction of Gaussian beams, which is useful for accurate modeling of small f-number beams and may be extended to modeling beams smoothed by phase plates.

An Etalon Integral (EI) method has been implemented to reconstruct the electric field at caustics of fold type. This method uses only ray quantities (phase, amplitude) without assumptions on local gradient scale length or wave angle with respect to the caustic. The caustic field is approximated by a sum of an Airy function and the derivative of an Airy function, which accounts for deviation from the simple Airy pattern observed in linear density profiles. Shortcomings of the base method have been identified in the case of dissipative media, for both GO and CGO. Subsequent adaptations have been proposed. Notably, the ray-ordering and root selection rules were adapted for the case of CGO in dissipative media. Calculations using IRT with GO and CGO in linear and nonlinear permittivity profiles have shown good agreement between the reconstructed fields with respect to reference solutions from the electromagnetic wave solver in *LPSE*. Notably, we have highlighted how GO cannot model caustic fields correctly very close to the caustic itself for dissipative media. This is related to attempting to model a complex caustic while retaining the approximation of small imaginary part of the ray phase. This phenomenon is correctly captured by CGO. In addition, we have shown that for sufficiently dissipative media, the caustic is fully embedded in complex space and no longer

N_rxN_yxN_θ	N_{tetras}	N_{vertices}	$N_{\text{ext. faces}}$	N_o	N_{lit}	t_{init} (s)	t_{step} (s)	t_{fields} (s)
51x3x51	4.2×10^5	7.9×10^3	108	676	301	14.3	6.4×10^{-2}	2.6×10^{-1}
101x3x101	1.6×10^6	3.1×10^4	108	2703	1192	64.5	2.2×10^{-1}	1.6
201x3x201	6.5×10^6	1.2×10^5	108	10706	4748	489.5	1.6	13.0
301x3x301	1.5×10^7	2.7×10^5	108	24009	10655	1745.2	5.7	46.9

TABLE II. Performance characteristics of *IFRIIT* calculations for the 2-D Gaussian density profile case. The various entries are the following: number of vertices in the simulation domain N_rxN_yxN_θ, number of tetrahedrons in the entire mesh N_{tetras}, number of vertices in the entire mesh N_{vertices}, number of external faces on the bounding mesh $N_{\text{ext. faces}}$, number of observation points N_o, number of observation points that have been determined to be on the lit side of the caustic N_{lit}, elapsed time for initialization of the IRT t_{init}, estimated elapsed time for timestepping of the IRT t_{step} and elapsed time for computation of the fields t_{fields}. All times are total CPU time.

manifests its influence in real space. In that case, the CGO framework is uniformly valid in the entire plasma and there is no caustic.

The IRT model, coupled with GO or CGO and formulated in the framework of a 3-D piecewise linear approximation based on tetrahedrons, has been implemented in the *IFRIIT* code. The code's capability to compute fields in a 2-D Gaussian density profile has been demonstrated. Notably, the model correctly predicts fields at caustics and in regions of high laser field refraction, two regions for which neither rigid-scale estimation, Paraxial Complex Geometrical Optics (PCGO), nor tessellation-based models converge natively to physical results. These results are obtained without the use of any artificial limitation coefficients or relaxation parameters. Model performances were discussed and are compatible with requirements for inline implementation into 3-D hydrodynamic codes. While GO and CGO have similar computational costs at fixed resolution, accurate field calculations in highly non-linear permittivity profiles with CGO require a finer meshing than with GO. This may be resolved by using piecewise permittivity functions that are smooth at interfaces, and will be explored in future work.

The *IFRIIT* model is formulated for convenient modeling of nonlinear LPI's. Notably, it will be used in conjunction with AMR to accurately model CBET at caustics.

VI. ACKNOWLEDGMENTS

This material is based upon work supported by the Department of Energy National Nuclear Security Administration under Award Number DE-NA0003856, the University of Rochester, and the New York State Energy Research and Development Authority.

This report was prepared as an account of work sponsored by an agency of the U.S. Government. Neither the U.S. Government nor any agency thereof, nor any of their employees, makes any warranty, express or implied, or assumes any legal liability or responsibility for the accuracy, completeness, or usefulness of any information, apparatus, product, or process disclosed, or represents that its use would not infringe privately owned rights. Reference herein to any specific commercial product, process, or service by trade name, trademark, manufacturer, or otherwise does not necessarily constitute or imply its endorsement, recommendation, or favoring by the U.S. Government or any agency thereof. The views and opinions of authors expressed herein do not necessarily state or reflect those of the U.S. Government or any agency thereof.

Appendix: The *IFRIIT* code framework

In this appendix, we give a brief description of the global workflow of *IFRIIT*, and discuss the current numerical cost of GO versus CGO.

1. Code structure

A simplified illustration of the *IFRIIT* working loop is given in Fig. 13. *IFRIIT* relies on rays to compute fields. As such, it describes continuously the medium in which the rays propagate, using a piecewise-linear approximation in 3D tetrahedrons. At initialization, the topology of the mesh must be computed; that is the 3D triangulation step. This triangulation may be unconstrained, e.g. when the code is used as a post-processor of a user-supplied point cloud, or constrained, e.g. when the code input is hydrodynamic data. During timestepping, the triangulation can be kept identical, even though the tetrahedron vertices may be moving. The IRT step is achieved by an iterative multi-dimensional Newton solver. The latter requires an initial guess to start iterations, whose quality is the main performance limitation of the IRT and *IFRIIT*. At initialization, the initial guess is computed from forward propagation of probe rays, and is in general not accurate. During timestepping, the initial guess is taken from the previous hydrodynamic step, which is in general an almost-converged guess.

The laser field is computed from the ray phases and amplitudes, and corrected by Etalon Integrals in order to produce physical fields at caustics of Fold type. Ray amplitudes are geometric factors that only depend on the topology of the permittivity map. For that reason, if LPIs do not modify the permittivity map, the IRT step and ray amplitude computation step only need to be

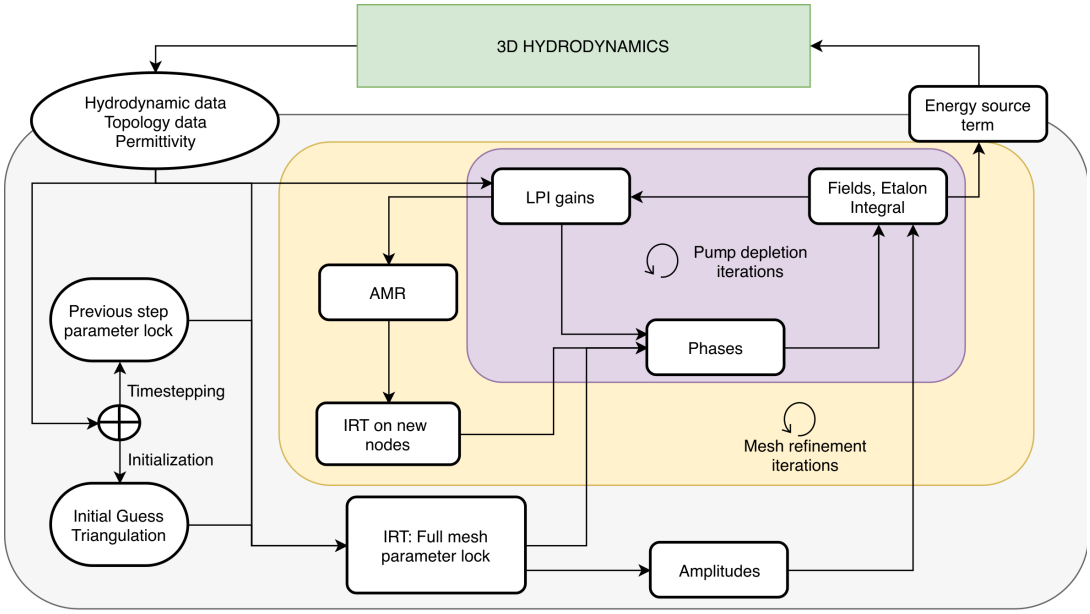

FIG. 13. Simplified workflow of a global iteration in *IFRIIT*. Main processes are shown in the grey box. Iterations pertaining to AMR steps are shown in the yellow box. Iterations pertaining to pump depletion steps are shown in the magenta box.

performed once per global iteration. In the CGO framework, that is generally not the case. However, preliminary studies suggest that it is a good approximation to neglect the contribution of LPIs to CGO ray propagation in most HEDP cases of interest. On the other hand, computation of the ray phase is conducted iteratively concurrently with the computation of LPI gain rates and of the laser field. This allows to account for pump depletion, that is important for accuracy of fields and energy conservation. The phase integration step is less expensive than the amplitude computation step, however, it must be repeated more often. Finally, global and local convergence of LPI gain rates, and energy conservation, may be achieved when necessary by adaptively refining the laser mesh in several AMR steps.

2. Use of CGO versus GO

Using CGO provides a more physical description of the laser propagation processes. Namely, it provides the most accurate representation of fields at caustics through laser refraction on the imaginary part of the permittivity, and allows to account for diffraction processes through the imaginary part of the beam phase. As such, from a model accuracy standpoint, the use of CGO appears preferred over that of GO.

The added numerical cost of CGO versus that of GO is not straightforward to estimate. CGO involves more numerous complex arithmetic operations, requires the use of a 6 dimensional Newton solver, involves more than twice the number of rays for computation of Jacobian matrices, and requires computation of complex momentum jump conditions between tetrahedrons in the piecewise-linear permittivity approximation. However, some of these added costs are also recovered in the IRT step itself. In GO, the most costly IRT-related operation is the determination that an observation point is in a caustic shadow. This is achieved by non-convergence of the Newton algorithm, i.e. by failing to find rays reaching a given point. Since CGO rays do reach the caustic shadow, this slower operation is not encountered and greatly speeds up the algorithm.

In general, we have found that CGO is only 0-30% slower than GO, even in the 2D Gaussian permittivity configurations. At the moment, the main drawback of utilizing CGO over GO is related to the description of permittivity as piecewise linear. This approximation produces discontinuities in complex space, that require ray jump conditions on the ray momentum. This loss of smoothness has been found to be detrimental to the accuracy of reconstructed fields in highly non-linear permittivity profiles such as the 2D Gaussian case considered in the paper, while this was not the case in simpler 1D cases. While this can be compensated with higher resolution meshing, this implies that CGO will then be significantly more costly. As such, efficient use of CGO in highly non-linear density profiles may require a piecewise description of the subgrid quantities that is smooth at interfaces. Such a description would be achieved at the cost of CPU efficiency. However, it is a planned development of the *IFRIIT* model that will be explored. It is theorized that these smoother permittivity profiles may also be beneficial to GO for accurate description of high-gain LPIs, which may be sensitive to numerical noise introduced by a continuous but non-smooth permittivity

map.

[1] J. Nuckolls, L. Wood, A. Thiessen, and G. Zimmerman. "laser compression of matter to super-high densities: Thermonuclear (ctr) applications". *Nature*, 239:139–142, September 1972.

[2] John Lindl. Development of the indirect-drive approach to inertial confinement fusion and the target physics basis for ignition and gain. *Physics of Plasmas*, 2(11):3933–4024, 1995.

[3] S. Atzeni and J. Meyer-ter Vehn. *The Physics of Inertial Fusion*. International Series of Monographs on Physics. Oxford University Press, Oxford, 2004.

[4] P. Michel, L. Divol, E. A. Williams, C. A. Thomas, D. A. Callahan, S. Weber, S. W. Haan, J. D. Salmonson, N. B. Meezan, O. L. Landen, S. Dixit, D. E. Hinkel, M. J. Edwards, B. J. MacGowan, J. D. Lindl, S. H. Glenzer, and L. J. Suter. Energy transfer between laser beams crossing in ignition hohlraums. *Physics of Plasmas*, 16(4), 2009.

[5] I. V. Igumenshchev, W. Seka, D. H. Edgell, D. T. Michel, D. H. Froula, V. N. Goncharov, R. S. Craxton, L. Divol, R. Epstein, R. Follett, J. H. Kelly, T. Z. Kosc, A. V. Maximov, R. L. McCrory, D. D. Meyerhofer, P. Michel, J. F. Myatt, T. C. Sangster, A. Shvydky, S. Skupsky, and C. Stoeckl. "crossed-beam energy transfer in direct-drive implosions". *Physics of Plasmas*, 19(5):056314, May 2012.

[6] A. Colaïtis, G. Duchateau, X. Ribeyre, and V. Tikhonchuk. Modeling of the cross-beam energy transfer with realistic inertial-confinement-fusion beams in a large-scale hydrocode. *Phys. Rev. E*, 91:013102, January 2015.

[7] S. Gus'kov, X. Ribeyre, M. Touati, J.-L. Feugeas, P. Nicolaï, and V. Tikhonchuk. "ablation pressure driven by an energetic electron beam in a dense plasma". *Physical Review Letters*, 109(25):255004, December 2012.

[8] A. Colaïtis, X. Ribeyre, E. Le Bel, G. Duchateau, Ph. Nicolaï, and V. Tikhonchuk. Influence of laser induced hot electrons on the threshold for shock ignition of fusion reactions. *Physics of Plasmas*, 23(7):072703, 2016.

[9] E. Llor Aisa, X. Ribeyre, G. Duchateau, T. Nguyen-Bui, V. T. Tikhonchuk, A. Colaïtis, R. Betti, A. Bose, and W. Theobald. The role of hot electrons in the dynamics of a laser-driven strong converging shock. *Physics of Plasmas*, 24(11):112711, 2017.

[10] T. B. Kaiser. "laser ray tracing and power deposition on an unstructured three-dimensional grid". *Phys. Rev. E*, 61:895, January 2000.

[11] D. J. Strozzi, D. S. Bailey, P. Michel, L. Divol, S. M. Sepke, G. D. Kerbel, C. A. Thomas, J. E. Ralph, J. D. Moody, and M. B. Schneider. Interplay of laser-plasma interactions and inertial fusion hydrodynamics. *Phys. Rev. Lett.*, 118:025002, Jan 2017.

[12] I. V. Igumenshchev, D. H. Edgell, V. N. Goncharov, J. A. Delettrez, A. V. Maximov, J. F. Myatt, W. Seka, A. Shvydky, S. Skupsky, and C. Stoeckl. "crossed-beam energy transfer in implosion experiments on omega". *Physics of Plasmas*, 17(12):122708, December 2010.

[13] J. A. Marozas, M. Hohenberger, M. J. Rosenberg, D. Turnbull, T. J. B. Collins, P. B. Radha, P. W. McKenty, J. D. Zuegel, F. J. Marshall, S. P. Regan, T. C. Sangster, W. Seka, E. M. Campbell, V. N. Goncharov, M. W. Bowers, J.-M. G. Di Nicola, G. Erbert, B. J. MacGowan, L. J. Pelz, J. Moody, and S. T. Yang. Wavelength-detuning cross-beam energy transfer mitigation scheme for direct drive: Modeling and evidence from national ignition facility implosions. *Physics of Plasmas*, 25(5):056314, 2018.

[14] A. Colatis, T. Chapman, D. Strozzi, L. Divol, and P. Michel. A tesselation-based model for intensity estimation and laser plasma interactions calculations in three dimensions. *Physics of Plasmas*, 25(3):033114, 2018.

[15] A. Colaïtis, G. Duchateau, P. Nicolaï, and V. Tikhonchuk. Towards modeling of nonlinear laser-plasma interactions with hydrocodes: The thick-ray approach. *Phys. Rev. E*, 89:033101, March 2014.

[16] Y. A. Kravtsov and N. Y. Zhu. *Theory of Diffraction, Heuristic Approaches*. Alpha Science Series on Wave Phenomena. Alpha Science International LTD., Oxford, U.K., 2010.

[17] R. K. Follett, D. H. Edgell, D. H. Froula, V. N. Goncharov, I. V. Igumenshchev, J. G. Shaw, and J. F. Myatt. Full-wave and ray-based modeling of cross-beam energy transfer between laser beams with distributed phase plates and polarization smoothing. *Physics of Plasmas*, 24(10):103128, 2017.

[18] Y. A. Kravtsov and Y. I. Orlov. *Caustics, Catastrophes and Wave Fields*. Springer, 1993.

[19] V. I. Arnold, S. M. Gusein-Zade, and A. N. Varchenko. *Singularities of Differentiable Maps, Volume 1*. Birkhäuser, 1988.

[20] C. G. Broyden. A class of methods for solving nonlinear simultaneous equations. *Math. Comp.*, 19:577–593, 1965.

[21] J. Liesen and Z. Strakos. *Krylov Subspace Methods, Principles and Analysis*. Numerical Mathematics and Scientific Computation. Oxford Science Publications, 2012.

[22] P. Maragos and R. Schafer. Morphological filters–part i: Their set-theoretic analysis and relations to linear shift-invariant filters. *IEEE Transactions on Acoustics, Speech, and Signal Processing*, 35(8):1153–1169, August 1987.

[23] J. E. Dennis Jr and R. B. Schnabel. *Numerical Methods for Unconstrained Optimization and Nonlinear Equations*. S.I.A.M., 1996.

[24] We have tested GMRES, FGMRES, Bi-CGStab and TFQMR methods.

[25] Alan C Hindmarsh, Peter N Brown, Keith E Grant, Steven L Lee, Radu Serban, Dan E Shumaker, and Carol S Woodward. SUNDIALS: Suite of nonlinear and differential/algebraic equation solvers. *ACM Transactions on Mathematical Software (TOMS)*, 31(3):363–396, 2005.

[26] W. L. Kruer. *The Physics of Laser Plasma Interactions*. Westview Press, University of California, Los Angeles, 2003.

[27] G. W. Forbes. On variational problems in parametric form. *American Journal of Physics*, 59(12):1130–1140, 1991.

[28] Roman A. Egorchenkov and Yury A. Kravtsov. Complex ray-tracing algorithms with application to optical problems. *J. Opt. Soc. Am. A*, 18(3):650–656, March 2001.

[29] Yu.A. Kravtsov. Iv rays and caustics as physical objects. volume 26 of *Progress in Optics*, pages 227 – 348. Elsevier, 1988.

[30] A.A. Asatryan and Yu.A. Kravtsov. Fresnel zones of hyperbolic type from the physical point of view. *Wave Motion*, 10(1):45 – 57, 1988.

[31] This is never the case in hot plasmas where electron-ion collisions are always present.

[32] Y. A. Kravtsov. "complex rays and complex caustics". *Radiophysics and Quantum Electronics*, 10:719–730, September 1967.

[33] D. Pesme, G. Bonnaud, M. Casanova, R. Dautray, C. Labaune, G. Laval, L. Bergé, and J.P. Watteau. *La fusion thermonucléaire inertielle par laser : l'interaction laser-matière part. 1, vol. 1. (French Edition)*. Synthèses. Eyrolles, 61, Boulevard Saint-Germain, 1993.

[34] J. F. Myatt, R. K. Follett, J. G. Shaw, D. H. Edgell, D. H. Froula, I. V. Igumenshchev, and V. N. Goncharov. A wave-based model for cross-beam energy transfer in direct-drive inertial confinement fusion. *Physics of Plasmas*, 24(5):056308, 2017.

[35] Joseph B. Keller and William Streifer. Complex rays with an application to gaussian beams. *J. Opt. Soc. Am.*, 61(1):40–43, January 1971.

[36] We have tested GMRES, FGMRES, Bi-CGStab and TFQMR methods.

[37] This is never the case in hot plasmas where electron-ion collisions are always present